

Brain-wide circuit interrogation at the cellular level guided by online analysis of neuronal function

Nikita Vladimirov^{1,4,6*}, Chen Wang^{1,6}, Burkhard Höckendorf^{1,6}, Avinash Pujala¹, Masashi Tanimoto^{1,2}, Yu Mu¹, Chao-Tsung Yang¹, Jason D. Wittenbach¹, Jeremy Freeman^{1,5}, Stephan Preibisch³, Minoru Koyama¹, Philipp J. Keller^{1,7*} and Misha B. Ahrens^{1,7*}

Whole-brain imaging allows for comprehensive functional mapping of distributed neural pathways, but neuronal perturbation experiments are usually limited to targeting predefined regions or genetically identifiable cell types. To complement whole-brain measures of activity with brain-wide manipulations for testing causal interactions, we introduce a system that uses measured activity patterns to guide optical perturbations of any subset of neurons in the same fictively behaving larval zebrafish. First, a light-sheet microscope collects whole-brain data that are rapidly analyzed by a distributed computing system to generate functional brain maps. On the basis of these maps, the experimenter can then optically ablate neurons and image activity changes across the brain. We applied this method to characterize contributions of behaviorally tuned populations to the optomotor response. We extended the system to optogenetically stimulate arbitrary subsets of neurons during whole-brain imaging. These open-source methods enable delineating the contributions of neurons to brain-wide circuit dynamics and behavior in individual animals.

Perturbing brain activity is indispensable for testing hypotheses about the contributions of individual neurons and circuits to brain function^{1–7}. Advances in optics and optogenetics have enabled concurrent neuronal imaging and 3D-targeted optogenetic manipulation^{3,8–11}, thus allowing the effects of neuronal stimulation on motor behavior and circuit activity to be monitored in larval zebrafish¹⁰. These methods typically target genetically defined cell types or predefined regions of the brain. However, even relatively simple behaviors are frequently generated by sets of neurons widely distributed across the brain^{12–14}, many of which may not be known in advance of an experiment. The activity patterns of all neurons, measured during the experiment through whole-brain imaging, could thus critically inform the choice of which neurons to perturb and allow models of distributed circuit function to be more exhaustively tested¹⁵. In addition, knowledge of brain-wide activity that results from a perturbation can be essential for mechanistically linking the perturbation to the evoked behavioral effects^{6,10,16,17}.

We sought to first measure neuronal activity in the entire brain and fit models to these data, then use these models to perturb any part of the brain and measure the brain-wide and behavioral effects of the perturbation to test hypotheses about circuit function, all in the same animal at single-cell resolution. To enable such experiments, we integrated whole-brain light-sheet microscopy^{18–20}, distributed computing²¹, and brain-wide two-photon optical perturbation. We directly coupled the experimental setup to a computer cluster that rapidly analyzed the data during the experiment. The results of such analyses, or ‘brain activity maps’²², can be used to select neurons on

the basis of their functional characterization and manipulate them at the single-cell level, while whole-brain functional imaging monitors the induced changes in brain activity.

We demonstrated the technique by using two modular, complementary approaches to perturb neuronal activity. In animals expressing a pan-neuronal calcium indicator, we ablated neurons tuned to specific aspects of a visually driven behavior. These manipulations had effects on behavior as well as long-range effects on brain activity. Second, we developed an optical system enabling simultaneous targeted two-photon optogenetic stimulation^{2,23} and whole-brain imaging (Opto-SiMView), through multiview light-sheet microscopy and concurrent spatially independent 3D two-photon point scanning. Stimulating functionally identified cells in multiple brain areas during light-sheet imaging, we observed brain-wide, distributed effects of optogenetic excitation. The systems were implemented as two separate microscopes to allow for simultaneous, parallel development of these complementary methods; their modular design makes them compatible with combined implementation as a single setup. The methods introduced here allow for activity and causality mapping at scales that were previously unattainable.

Results

Experimental and computational setup. A zebrafish larva expressing a genetically encoded calcium sensor in almost all neurons in its brain was placed in a virtual-reality environment where it could fictively perform a variety of behaviors²⁰ (Fig. 1a, left). We

¹Janelia Research Campus, Howard Hughes Medical Institute, Ashburn, VA, USA. ²Nagoya University, Nagoya, Japan. ³Berlin Institute for Medical Systems Biology (BIMSB), Max Delbrück Center for Molecular Medicine in the Helmholtz Association (MDC), Berlin, Germany. ⁴Present address: Berlin Institute for Medical Systems Biology (BIMSB), Max Delbrück Center for Molecular Medicine in the Helmholtz Association (MDC), Berlin, Germany. ⁵Present address: Chan Zuckerberg Initiative, San Francisco, CA, USA. ⁶These authors contributed equally: Nikita Vladimirov, Chen Wang, Burkhard Höckendorf.

⁷These authors jointly supervised this work: Philipp J. Keller, Misha B. Ahrens. *e-mail: nikita.vladimirov@gmail.com; kellerp@janelia.hhmi.org; ahrensm@janelia.hhmi.org

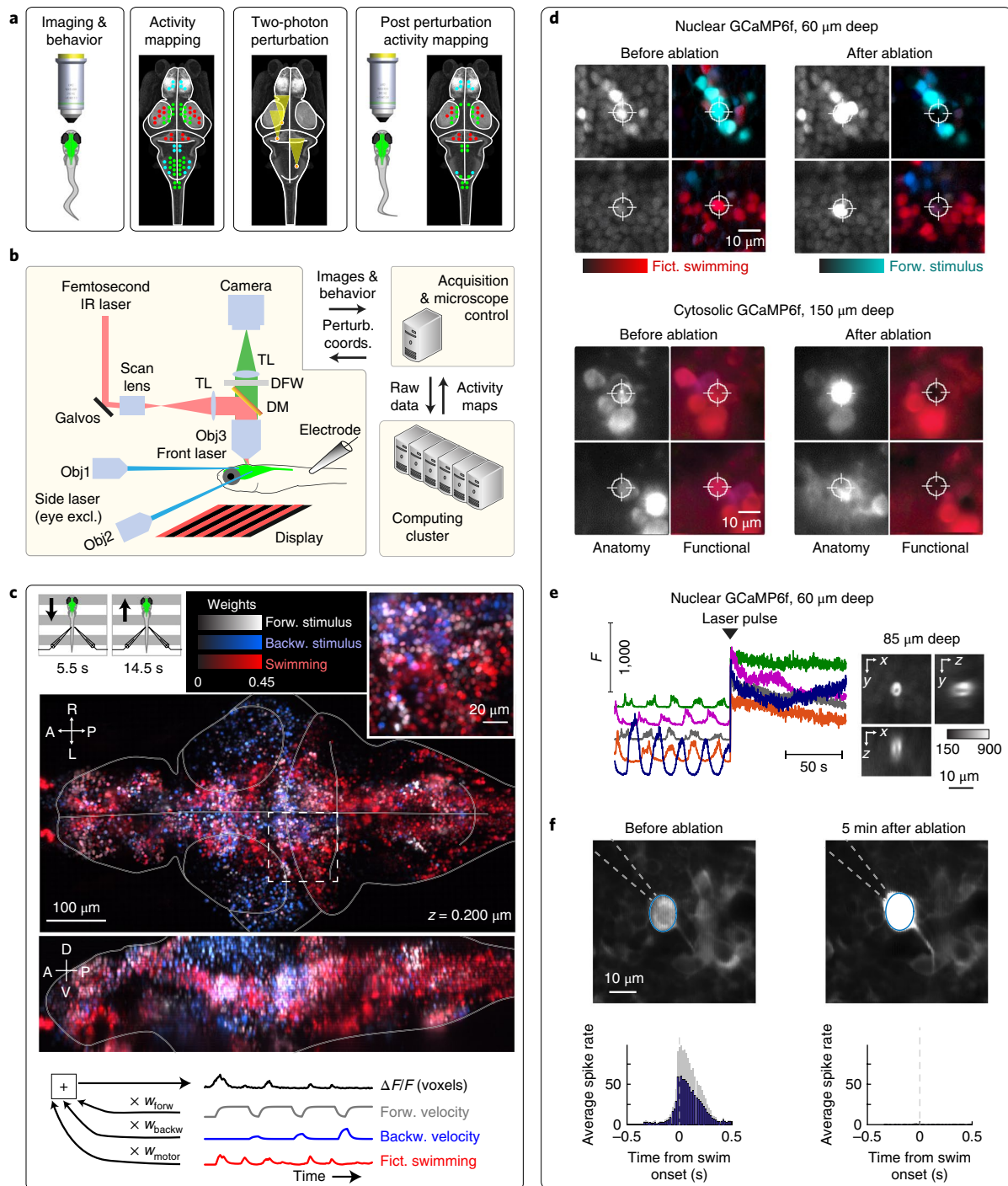


Fig. 1 | Experiment workflow, analysis, and ablation demonstration. **a**, Overview of the technique. **b**, Implementation of the experimental and analysis setup. A light-sheet microscope records whole-brain activity in larval zebrafish fictively behaving in a virtual-reality system⁴⁷. A pulsed infrared (IR) laser is targeted to the brain for single-cell ablation. Obj, objective; TL, tube lens; DM, dichroic mirror; DFW, detection filter wheel; excl., excluded; perturb. coords., perturbation coordinates. **c**, Analysis of brain activity during the optomotor response. Whole-brain activity was analyzed by linear regression against the stimulus and behavior (bottom), thus generating an activity map showing each voxel's tuning to forward (forw.) and backward (backw.) motion stimulus and swimming. For *Tg(elavl3:H2B-GCaMP6f)*¹⁷ fish 6 dpf, similar brain maps were observed in analyses of more than 50 other fish. A, anterior; P, posterior; R, right; L, left; D, dorsal; V, ventral; fict., fictive. **d**, Examples of ablations of functionally identified cells, two in fish expressing GCaMP6f in the nucleus (left, *Tg(elavl3:H2B-GCaMP6f)*) and two in fish expressing GCaMP6f in the cytosol (right, *Tg(elavl3:GCaMP6f)*). In the calcium measurements (grayscale), an increase in brightness follows the ablation. The functional maps (colored) show that the tuning of the cells to the stimulus and motor output disappears. **e**, Imaging from neurons in a behaving animal during ablation. *F*, fluorescence intensity of individual neurons over time. Right, ablation is typically localized to a single cell, as shown in the projections of the postablation cell (GCaMP6f expressed in the nucleus). **f**, Electrophysiological verification of loss of spiking after cell ablation. nMLF cells (MeL, 5 cells in 5 fish) were recorded with a loose-patch electrode in *Tg(elavl3:GCaMP6f)* fish and showed spiking before cell ablation (black bars, mean firing rate across cells; gray bars, s.e.m.). Nontargeted cells still showed activity (Supplementary Fig. 1b).

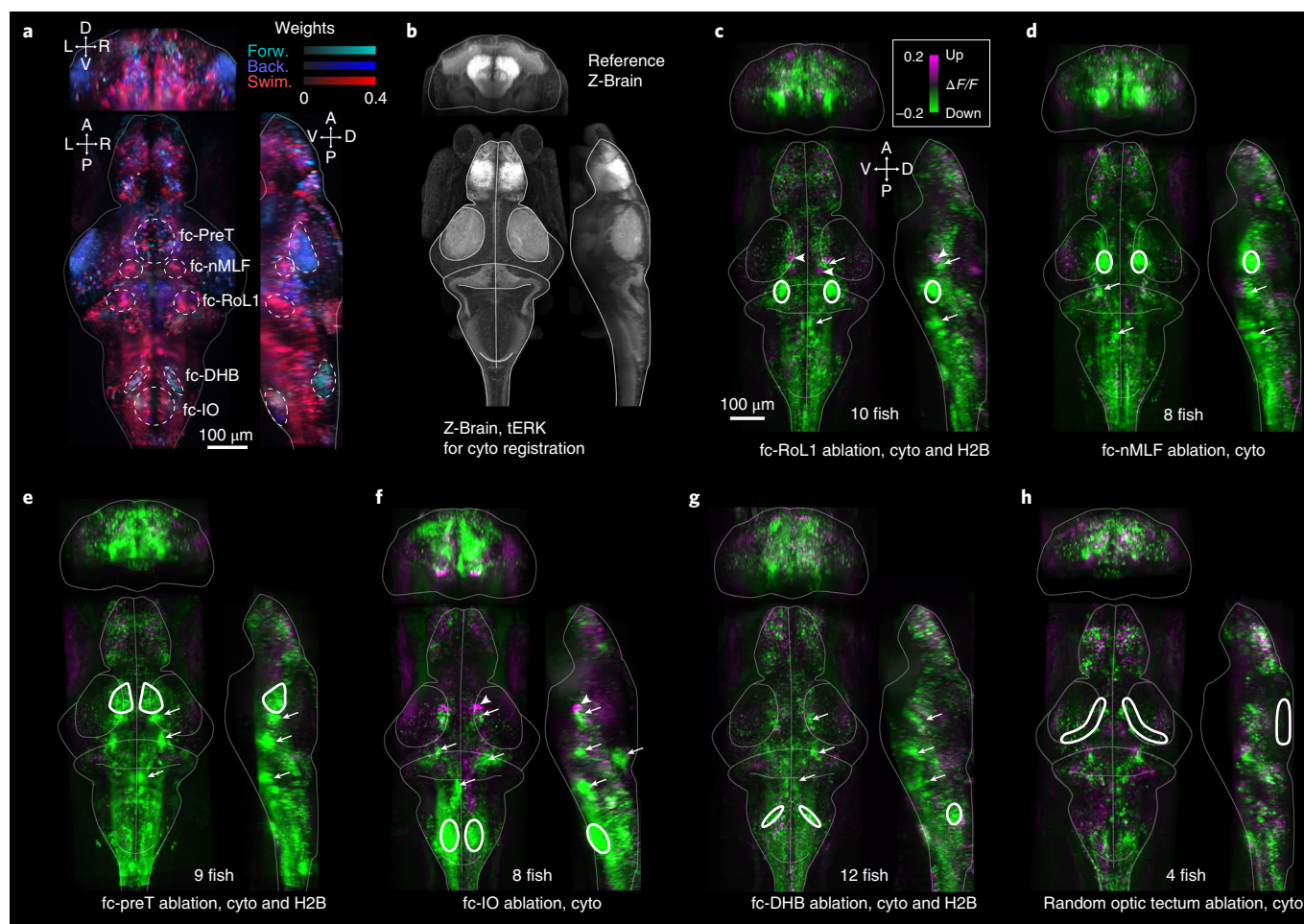


Fig. 2 | Effects of targeted ablations on whole-brain activity. **a**, Functionally active neuronal clusters chosen for ablations. A functional map of one representative fish is shown (out of more than 100 repeat experiments), with the selected clusters outlined in white. The clusters are named according to their approximate location to known areas. The fc-RoL1 area includes RoL1 reticulospinal neurons and the locus coeruleus (LC) neurons. **b**, Reference Z-Brain³¹ (showing tERK staining) used for nonrigid cross-fish registration. **c–h**, Differences in $\Delta F/F$, averaged over the forward-stimulus period, before and after targeted ablations. Green indicates a decrease in activity after ablation. Multiple brains are aligned to reference brains from the Z-Brain resource³¹. Brains from fish expressing nuclear-localized and cytosolic GCaMP6f were merged. Regions of cell ablation are outlined in white. In **c–f**, neurons tuned to the swimming were ablated; in **g**, neurons tuned to forward visual motion were ablated; in **h**, cells were randomly ablated (white contours). **c–g**, Arrows point to decreases in activity. Arrowheads indicate increases in activity. Cyto refers to the *Tg(elavl3:GCaMP6f)* transgenic fish, and H2B refers to *Tg(elavl3:H2B-GCaMP6f)*.

imaged its entire brain with a light-sheet microscope (Zebrascop, Supplementary Table 1) to record the activity of individual neurons during behavior. Using cluster computing through the Thunder analysis framework²¹, we quickly analyzed these whole-brain data while the experiment was ongoing (processing times depending on cluster sizes in Supplementary Table 2), generating whole-brain activity maps describing properties of neurons such as tuning to visual stimuli and relationships to behavior. From this map, we selected up to several hundred individual neurons for deletion, according to their tuning properties, location, and (optionally) coexpression of genetic markers. These neurons were then targeted for rapid deletion by two-photon plasma ablation through a pulsed infrared laser in the microscope detection pathway (Fig. 1a, middle). We then imaged the fictively behaving fish again (Fig. 1a, right) to analyze differences in brain activity and behavior. The experimental–computational setup is schematized in Fig. 1b. Next, to enable gain-of-function experiments through optogenetic activation, we developed a modular system for Opto-SiMView (Supplementary Table 3). Volumetric imaging was mechano-optically decoupled from a 3D-scanned two-photon excitation beam focus with an electrically

tunable lens (ETL), so that a given set of points in three dimensions could be continuously stimulated during whole-brain imaging, without sacrificing optical performance in the imaging process.

Behavioral paradigm. For a test bed for this system, we made use of a robust innate behavior, the optomotor response (OMR), in which fish swim forward when presented with a forward-moving visual stimulus²⁴ (5.5 s of variable-speed backward visual motion (which makes the fish swim less), 1.1 s of a stationary visual stimulus, and 14.5 s of variable-speed forward visual motion (which makes the fish swim more), repeated for 10 min). We imaged the entire brain of the fish during this behavior with light-sheet microscopy²⁰ (Fig. 1c).

Whole-brain activity maps. To create whole-brain activity maps, we used linear-regression analysis^{13,25} to map the tuning of every voxel in the dataset to three variables: the backward velocity of the visual stimulus, the forward velocity of the stimulus, and the instantaneous swim power (Fig. 1c). Every voxel was assigned three weights (w_{backward} , w_{forward} , and w_{motor}) which are regression coefficients depicted

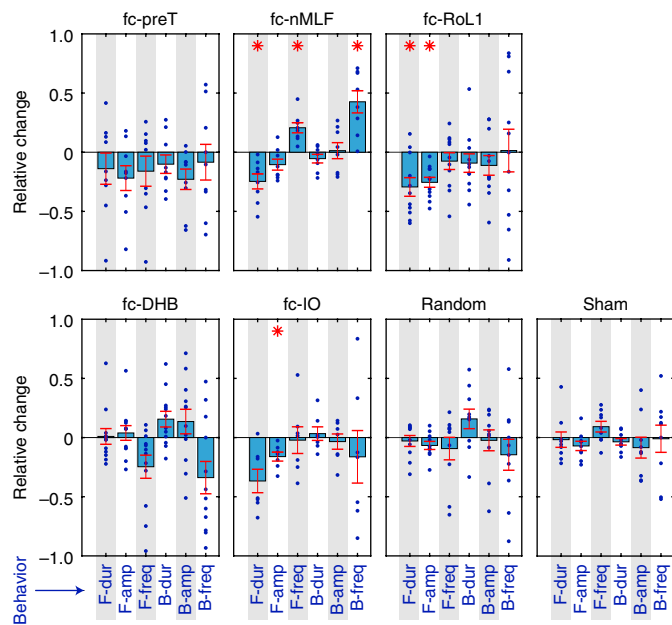


Fig. 3 | Differences in behavior after targeted ablations. For each area in which neurons were ablated (motor tuned in regions fc-preT, fc-nMLF, fc-RoL1, and fc-IO; motor/sensory tuned in fc-DHB), six behavioral measures are shown (average duration of individual swim bouts (dur), amplitude of swim bouts (amp), and swim-bout frequency (freq), during both forward (F-) and backward (B-) stimuli). Statistical significance was assessed with two-tailed *t* tests on the relative change $(x_{\text{post}} - x_{\text{pre}})/(x_{\text{post}} + x_{\text{pre}})$, and statistical significance, indicated by red stars, was determined with a shuffle test to control the FWER to 0.05 per lesioned area (Methods). The random and sham control ablations did not generate significant behavioral effects (under a FWER of 0.05). Each plotted point represents one fish.

after being multiplied by a ‘goodness of fit’ measure (R^2) to emphasize well-fit neurons and scaled by a gamma correction of 0.5 (i.e., the square root of pixel brightness) for easier visualization, thus describing how well the stimulus and the behavior predicted the activity of the voxel over time. Within minutes, this procedure generated whole-brain maps of the weights, color-coded in red (swimming), grayscale (forward stimulus), and blue (backward stimulus) (Fig. 1c and Supplementary Videos 1 and 2), thus revealing sets of neurons tuned to swimming and/or to the stimuli (functional maps). These functional maps formed a basis for selecting neurons targeted for deletion.

Neuronal ablation. To verify that we were able to delete individual neurons identified by using brain activity maps, we used a custom-written ImageJ plugin to manually select neurons in various parts of the brain, then targeted them for two-photon plasma ablation (Fig. 1d). We optimized the cell-ablation protocol for achieving single-cell resolution^{1,24,26,27} by using a short 2- to 3-ms exposure to a high-power pulsed femtosecond laser (930 nm, 500 mW after the objective) focused on the center of a cell. After the exposure, the brightness of the cell increased immediately (Fig. 1e), presumably indicating the release of intracellular calcium after the destruction of intracellular organelles or the influx of external calcium after the rupture of the cell membrane; the brightness eventually decreased. The short exposure time of our protocol allowed us to avoid cavitation (formation of vapor bubbles) in the tissue; direct laser damage is likely to be restricted to a punctate volume within the soma (Fig. 1e, right). In addition to the increase in overall brightness, the voxels in targeted cells became untuned, thus losing any correlation to the stimulus and motor variables (Fig. 1d, Supplementary

Video 3 and Supplementary Fig. 1). In more than 90% of cases (~90% in deep brain areas more affected by scattering, and >90% in more dorsal brain areas), neighboring cells retained their activity patterns. The ablation protocol was successful in zebrafish at both 5 and 6 d postfertilization (dpf) zebrafish expressing GCaMP6f in the cytosol (*Tg(elavl3:GCaMP6f)*) or in the nucleus (*Tg(elavl3:H2B-GCaMP6f)*), although nucleus-expressing neurons were ablated more reliably and consistently than neurons with cytosolic expression. Electrophysiological recordings confirmed that under this ablation protocol, the ablated cell stopped spiking (presumably because of cell death; Fig. 1f), but neighboring cells still showed activity (Supplementary Fig. 1b). As an additional control for the spatial specificity of ablation, we verified that ablation of the Mauthner cell (M cell), known to mediate escape responses²⁸, led to expected changes in escape latency, but ablation of nearby cells (seven or eight cells within 20 μm) did not (Supplementary Fig. 1c).

Whole-brain causal mapping through optical neuron deletion.

We demonstrated this technique by targeting neurons tuned to specific aspects of optomotor behavior in a set of five brain areas chosen because they showed robust, reproducible clusters of cells tuned to motor output or sensory input. In these regions, we targeted cells with specific functional signatures (such as tuning to motor output) (Fig. 2a, areas indicated by white dashed lines). For simplicity of terminology and in recognition of our focusing on functionally identified cells rather than a strict anatomical cell-type-specific delineation, we refer to these areas as functional clusters (fc), defined according to their proximity and resemblance to known brain areas^{29,30}; these clusters may not fully intersect with anatomically defined regions, because our method is based on activity maps (for instance, they may cover a superset, subset, or a specific functional cell type). For example, f-nMLF overlaps with the nucleus of the medial longitudinal fasciculus (nMLF), although it is somewhat more lateral^{29,31,32} (Supplementary Fig. 2); fc-IO overlaps with the inferior olive (IO); fc-RoL1 overlaps with the RoL1 reticulospinal neurons and the locus coeruleus (Supplementary Fig. 2); and fc-preT overlaps with the pretectum (preT). In addition, we targeted forward-motion-selective neurons in the dorsal hindbrain (DHB)²¹ (fc-DHB, cyan cells in Fig. 2a). We also included, as a control, randomly localized ablations of similar numbers of cells in the optic tectum, an area known not to be necessary for the OMR³³. We targeted ~120 cells per area. The brains were nonrigidly registered to a reference brain³¹ for visualizing population results (Fig. 2b).

Deleting clusters of functionally defined neurons in these brain areas had profound effects on widespread brain activity (Fig. 2c–g and Supplementary Video 4). First, ablating motor-tuned cells in fc-IO (Fig. 2f and Supplementary Fig. 3a,b) affected wider hind-brain activity including in the dorsal layers of the cerebellum, in agreement with known anatomical connections. Deletions of functionally defined neurons in other brain areas also had a large effect on brain-wide dynamics (Fig. 2c–g)—primarily decreases in activity in the hindbrain and midbrain. Ablations in the optic tectum of randomly selected neurons resulted in smaller changes in brain activity during the optomotor task (Fig. 2h).

We quantified the effects of the deletions on behavior in the optomotor assay through multiple behavioral measures: swim duration, swim amplitude, and swim frequency, during both the forward and backward stimulus. We tested for statistically significant relative changes $(x_{\text{post}} - x_{\text{pre}})/(x_{\text{post}} + x_{\text{pre}})$ (where x indicates a behavioral measure), using two-tailed *t* tests with a significance threshold adjusted for multiple comparisons to control the family-wise error rate (FWER) per brain area to be 0.05. Ablation of motor-tuned neurons in the fc-nMLF, fc-RoL1, and fc-IO areas decreased swim vigor, but ablation of motor-tuned neurons in fc-nMLF resulted in an increase in swim-bout frequency (Fig. 3). Thus, function-targeted ablations resulted in measurable changes in specific behavioral parameters.

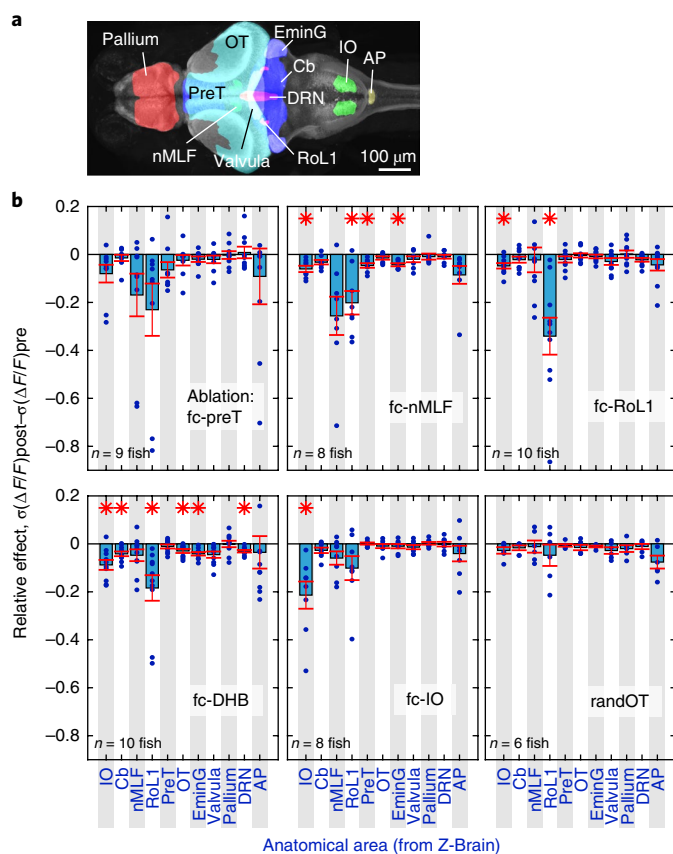


Fig. 4 | Brain dynamics in known anatomical areas from reference brain before and after ablation of functionally defined areas. a, Projections of 11 selected anatomical brain areas from the Z-Brain atlas used for brain activity analysis. **b**, Relative changes in brain dynamics in the 11 anatomical brain areas after ablation of the five functionally defined brain areas, quantified by the change in s.d. of $\Delta F/F$ in the regions of interest over the course of the experiment, $\sigma(\Delta F/F)_{\text{post}} - \sigma(\Delta F/F)_{\text{pre}}$. Asterisks indicate significance at 0.05 FWER per lesioned brain area (details of multiple-comparisons correction in Methods), two-tailed t test and Wilcoxon signed-rank test. Cb, cerebellum; OT, optic tectum; EminG, eminentia granularis; AP, area postrema; randOT, random optic tectum ablation.

Next, we statistically quantified the global changes in neuronal activity (Fig. 2), using known anatomical-mask overlays of the Z-Brain zebrafish brain atlas³¹, from which we selected 11 regions of interest: the preT, nMLF, RoL1, cerebellum, IO, optic tectum, eminentia granularis, valvula, pallium, superior (dorsal) raphe, and area postrema (Fig. 4a). We applied inverse nonrigid transformations to the reference masks and mapped them onto individual fish brains. The brain activity in the areas covered by the masks (ninety-fifth-percentile $\Delta F(t)/F_0(t)$, where F is fluorescence intensity and t is time, over all voxels in the region of interest for every time point), plotted for exemplary fish showed that changes in brain dynamics occurred after ablation (Supplementary Fig. 3c).

To statistically quantify the relative effects of the ablation of functional cell types in specified brain areas, we calculated the relative change in the s.d. of neural activity measurements before and after ablation, $\sigma(\Delta F/F)_{\text{post}} - \sigma(\Delta F/F)_{\text{pre}}$. We assessed statistical significance with two-tailed t tests with a significance threshold adjusted for multiple comparisons. Figure 4b shows the relative effect of ablating cells in the five brain areas selected by their activity (plus one control region in the optic tectum) on the 11 anatomically selected brain areas.

The random cell ablations in the optic tectum resulted in minor changes in the activity variance in other brain areas during the OMR. In contrast, ablation of fc-nMLF, fc-RoL1, fc-DHB, and fc-IO caused significant changes across multiple brain areas (Fig. 4b). The effects of ablations in fc-preT showed trends in multiple areas, but these did not reach significance. In summary, we observed that ablation of functional clusters gave rise to widespread changes in activity, primarily suppressive, across the brain. The OMR appeared to be sufficiently robust to not be eliminated by these perturbations, despite the changes in brain activity and specific aspects of behavior.

Whole-brain causal mapping through neuronal optogenetic activation.

To incorporate gain-of-function capabilities through cellular-level optogenetic excitation, we developed a microscope capable of independently targeting locations throughout a 3D volume for two-photon stimulation, while volumetric data were acquired with a light-sheet system^{34–36} (Opto-SiMView, Supplementary Table 3, Fig. 5a and Supplementary Data 1 and 2). We opted for a piezopositioned, shared objective for 3D imaging and excitation to ensure optimal diffraction-limited resolution and the highest light transmission in the detection arm. We descanned the objective movement in the excitation arm by using an ETL to keep locations targeted with the focused infrared femtosecond laser beam stationary inside the sample (Fig. 5a), with minimal aberrations and uniform, high focus quality across the entire 3D imaging volume ($830 \times 415 \times 200 \mu\text{m}$ imaged at 3 Hz). To excite any set of neurons during whole-brain imaging, a two-photon excitation focal spot hops around the brain, steered by an x - y galvanometer scanner and the ETL. To rapidly target different locations while precisely compensating for objective motion, we developed a custom high-speed ETL driver with 20- μs temporal resolution and 7.5- μA operating current resolution and a closed-loop optimization method for tuning the ETL waveform (Supplementary Fig. 4 and Supplementary Data 2). The resulting 3D position error was less than $1 \mu\text{m}$ throughout the brain volume (Fig. 5b). The excitation optics were configured for a z range of $\sim 400 \mu\text{m}$ and a lateral and axial point-spread function (PSF) size of 1.5 and $9.5 \mu\text{m}$, respectively (Fig. 5c,d). An experimental demonstration and characterization of the spatial confinement of photomanipulation in vivo, targeting individual cells across the larval zebrafish brain, was also performed (Supplementary Figs. 5 and 6).

Opto-SiMView is capable of stimulating dozens of neurons in distributed locations across the brain during each volume scan. For concurrent optogenetic stimulation and imaging, we used fish expressing the calcium indicator jRGECO1b³⁷ and optogenetic channel CoChR²³ in almost all neurons (*Tg(elavl3:jRGECO1b); Tg(elavl3:CoChR-eGFP)*, Supplementary Fig. 7).

To demonstrate the brain-wide effects of optogenetic excitation during whole-brain imaging, we stimulated cells in three brain areas: the dorsal raphe nucleus (DRN), the nMLF, and the IO. Stimulating cells in the DRN (Fig. 6a) showed prolonged excitation of the DRN and faster activation in the IO, a result consistent with the slow timescales observed in serotonergic cells in the DRN³⁸ and the known serotonergic modulation of IO activity³⁹, respectively. We observed decreases in calcium levels in the cerebellum. Replicates, controls targeting regions just outside the brain, controls with a transgenic line lacking CoChR and a characterization of manipulation confinement are shown in Supplementary Figs. 8–11 and Fig. 6.

When stimulating the IO, we observed increased as well as decreased activity in the cerebellum (examples of increased activity in Fig. 6b and Supplementary Fig. 8b), in agreement with IO projections to Purkinje cells in the cerebellar cortex⁴⁰ and inhibitory projections from Purkinje cells to cerebellar eurydendroid cells in fish⁴¹.

When stimulating the nMLF (Fig. 6c and Supplementary Fig. 8c), we observed widespread brain activation in the cerebellum, DRN, and IO. Upward calcium deflections in the IO were consistent with

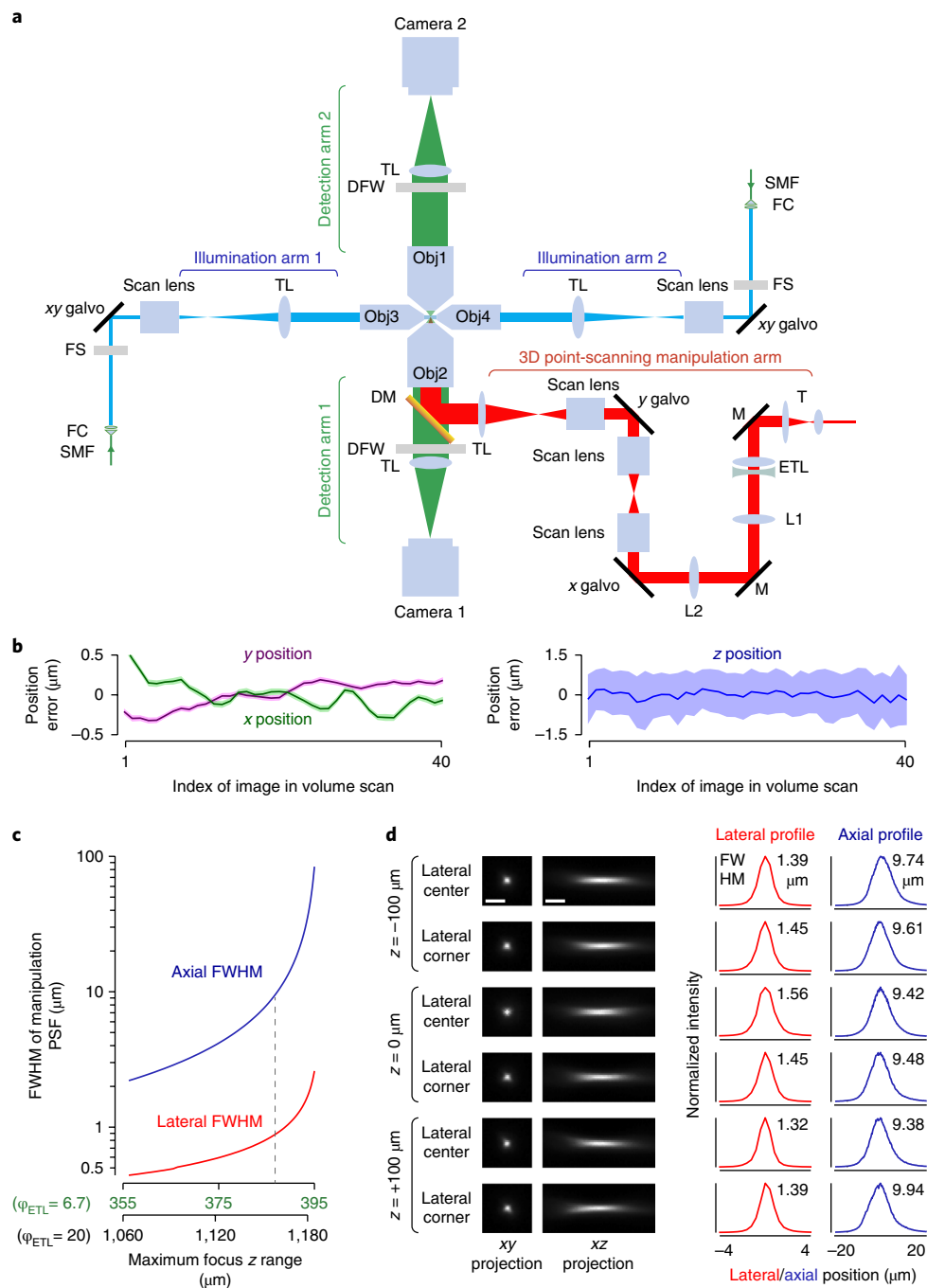


Fig. 5 | Opto-SiMView microscope design for concurrent volumetric imaging and 3D optical manipulation. **a**, Optical layout of the multiview light-sheet microscope with ETL-based 3D optical manipulation arm (Opto-SiMView). The SiMView arrangement^{34,35} provides two-sided illumination, two-sided detection, and adaptive imaging capabilities³⁶. For optical manipulation, a femtosecond laser is coupled into detection arm 2, and the 3D focus position is controlled laterally (x, y) by galvanometer scanners (xy galvo) and axially (z) by the ETL, independently of the objective position. SMF, single-mode fiber; FC, fiber coupler; FS, filter wheel and shutter; TL, tube lens; DFW, detection filter wheel; T, telescope; M, mirror; L1, lens 1; L2, lens 2. **b**, Lateral (left) and axial (right) position error of 3D focus generated by the optical-manipulation arm during high-speed piezo-based volumetric imaging (40 images per volume, 3-Hz volume rate, 200-μm z range). Plots show mean values (solid lines) and s.d. (light-colored patches, $n=100$ volume scans) of the spatial distance between the intended and measured focus positions as a function of time during the volume scan. **c**, Approximate theoretical relationship between two-photon focal-spot size and the maximum z range of the ETL setup, obtained by varying beam size while maintaining constant magnification between the objective and ETL. The dashed gray line indicates the configuration used here. FWHM, full width at half maximum; φ_{ETL} , optical power of ETL. **d**, Measurement of manipulation PSF with fluorescein dye at different positions in the volume (in vivo characterization in Supplementary Figs. 5 and 6). For 0.4 numerical aperture, PSF quality (images to left) and size (plots to right) are shown across the 200-μm-deep imaging volume. The experiment shown in this figure was repeated independently three times with similar results. Scale bars, 5 μm (**d**).

and opposite from ablation results (Fig. 4b). The effect on the DRN was not opposite from that of nMLF ablation, suggesting that ablation and stimulation effects are not always opposite, as expected

from the intricacy of communication in neural circuits, and demonstrating the benefit of using both. When stimulating the nMLF, we also observed responses in the tectum (Fig. 6c).

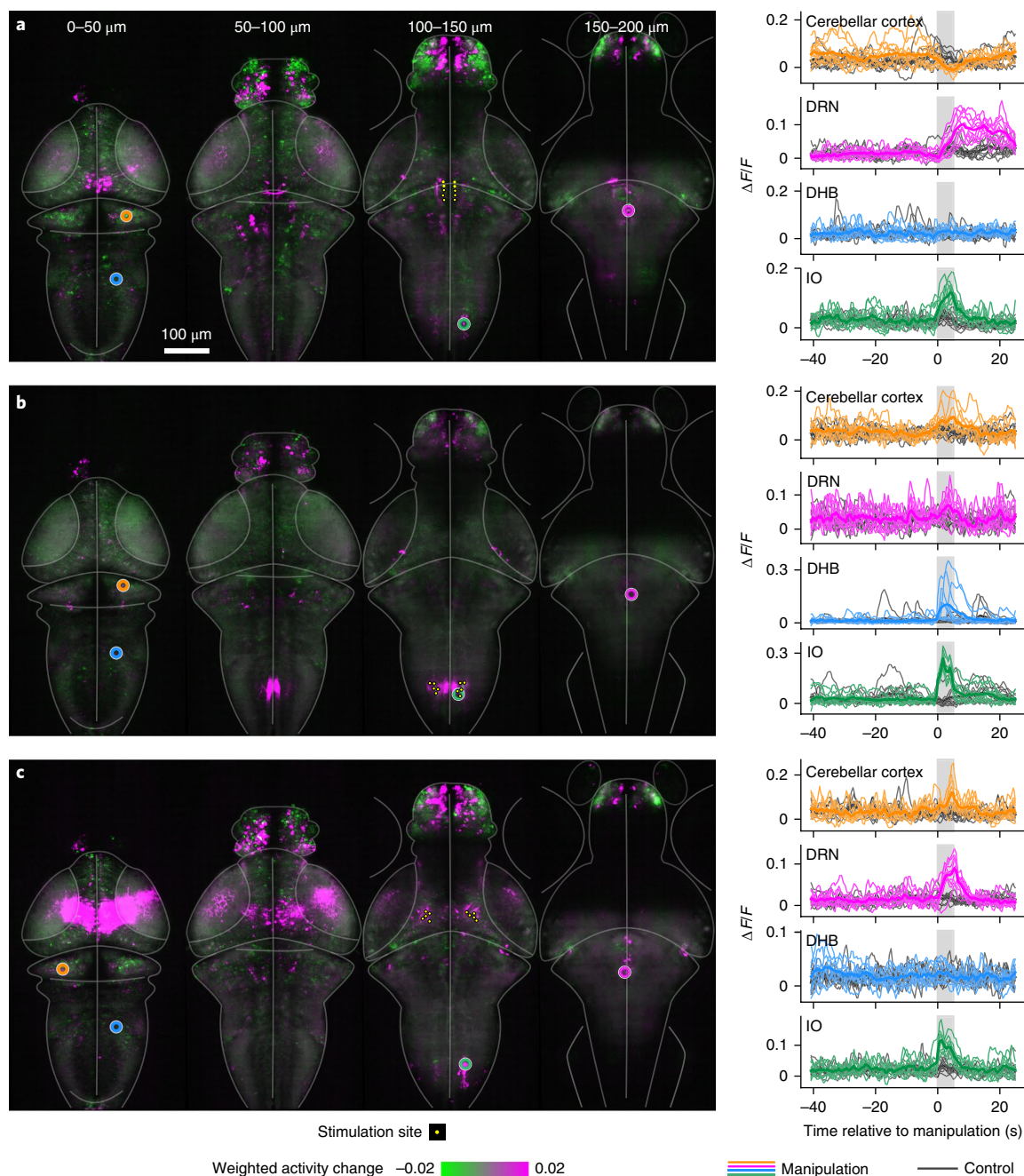


Fig. 6 | Targeted optogenetic excitation causes brain-wide responses. a–c, Optical manipulation of cells in the DRN (**a**), IO (**b**), and nMLF (**c**) during volumetric functional imaging of transgenic line *Tg(elavl3:jRGECO1b) × Tg(elavl3:CoChR-eGFP)*. Left, targeted cells are indicated by yellow dots, and locations of example cell responses are indicated by open circles. Shown are four maximum-intensity projections, each covering a successive 50- μm z interval of the full image volume. Control manipulations were targeted to a set of points outside the brain. The color code shows the weighted activity change relative to control manipulations to normalize for activity fluctuations not locked to the neuronal stimulation. Activity measures are averaged across ten trials (for the same specimen, a replicate of this series of experiments in a second specimen is shown in Supplementary Fig. 8; in total, the experiment shown in this figure was repeated independently three times with similar results). Right, $\Delta F/F$ time traces of the indicated positions (left), showing the activity profile of selected single cells (orange, magenta, blue, and green) located in the cerebellum, DRN, DHB, and IO. Traces are shown for all trials (thin colored lines) and controls (thin black lines). Thick lines represent mean traces.

Functional activity maps can be combined with genetically expressed markers, such that targeted manipulations can be chosen according to both neuronal activity patterns and cell type. We demonstrated this combination by using double-transgenic fish expressing nuclear-localized GCaMP6f and fluorescent markers in glutamatergic or GABAergic cells, allowing neurons to be classified according to both function and neurotransmitter phenotype

(Supplementary Fig. 2a,b). In addition, spinal cord backfills were performed to localize functionally defined populations to known reticulospinal neurons (Supplementary Fig. 2c).

Discussion

Neurons in brain circuits represent different environmental, bodily, and cognitive variables, and interact to mediate behavior.

Understanding these circuit interactions requires perturbing neural activity representing the relevant variables. These neural representations do not always overlap with specific genetically defined cell types, may not always be contained in a delineated brain region, and may differ among individual animals. The approach introduced here allows researchers to first identify in a locus-agnostic way which neurons represent the behaviorally relevant variables and then, by choosing which of those neurons to perturb, to test whether and how any given representation is used by the wider circuit to orchestrate behavior.

A recent complementary approach to mapping the contributions of neurons to brain dynamics and behavior in larval zebrafish has similarly made use of combined imaging and stimulation setups, integrating two-photon parallel 3D holographic optogenetic stimulation with two-photon volumetric imaging, behavioral monitoring, and a different (complementary) computational strategy¹⁰. In that study, the contributions of neurons in an identified nucleus to behavior were analyzed by stimulating different subsets of cells and using an algorithm to narrow down the most important sets of neurons for generating specific tail movements. Concurrent two-photon imaging allowed for large populations of neurons to be monitored for activity induced by the optogenetic excitation.

In mammals, combined two-photon-based imaging and perturbation systems have been developed and applied to the hippocampus and cortex^{3,8,9,11}. The choice of which cells to stimulate can be based on the tuning of cell activity⁹; furthermore, the dependence of the effect on behavior on the particular wider neuronal population that is recruited can be determined¹¹, thus demonstrating the utility of combined imaging and perturbation in clarifying circuit function.

We used a computer cluster to handle the high data rates of whole-brain imaging, but adaptations of the computational framework—for example, fast segmentation of neurons to reduce the data from $\sim 10^8$ voxels to $\sim 10^5$ neurons—would enable similar analysis to run on a workstation. Such preprocessing would also simplify fitting models to the data that are more complex than the linear models used here. Furthermore, the step of choosing which neurons to target, here done manually on the basis of activity maps, could be absorbed into the computational pipeline; for example, by applying an efficient combinatorial search¹⁰ through a functionally identified set of neurons.

We designed the Opto-SiMView optical manipulation system to optimize image quality during stimulation. Combining light-sheet imaging and optogenetic excitation would in principle be easiest via a stationary objective, by using swept confocally aligned planar excitation (SCAPE)⁴², spherical aberration-based axial PSF elongation (SPED)⁴³, cubic-phase masks⁴⁴, or ETL⁴⁵ configurations for volumetric imaging. However, the advantages of imaging with a stationary objective (and in the case of SCAPE, removing the need for a separate illumination objective) come at the expense of image quality, since these techniques image the sample away from the native focal plane of the objective and (with the exception of the ETL system) rely on mechanisms that reduce axial resolution. Opto-SiMView therefore employs a moving objective for volumetric imaging and an optically more complex two-photon excitation arm for concurrent but independent 3D manipulation via the same objective. As a result, the Opto-SiMView detection system provides high photon efficiency, minimal aberrations, and high resolution. Opto-SiMView also enables neuron ablation, although it is more elaborate to build, and our simpler, ETL-free ablation system Zebrascope is sufficient when concurrent 3D imaging and optical manipulation are not needed. Conversely, the latter system can also be used for optogenetic excitation, but only in the plane imaged by the detection system. Owing to these tradeoffs between complexity and versatility, we included both systems in this report.

We used neuron ablation, optogenetic neuronal activation, and optical labeling through photoactivatable GFP^{46,47} (which has also been used before to visualize the morphology of holographically

stimulated neurons in zebrafish¹⁰) to demonstrate our approach, but the workflow is equally applicable to other light-based manipulations, such as light-activated gene expression⁴⁸.

The behavioral effects of the ablations extend the understanding of visuomotor transformations of zebrafish. The decrease in motor vigor seen after the deletion of motor-tuned neurons in fc-RoL1, which includes the RoL1 reticulospinal neurons and the locus coeruleus, is consistent with the known involvement of reticulospinal neurons in the generation of swim bouts²⁴ and the function of the locus coeruleus in controlling arousal^{49,50}. In contrast, ablation of motor-tuned neurons in fc-nMLF, which is known to play a role in swimming and posture control^{10,24,32,51,52}, caused an increase in swim frequency, a finding opposite from what might naively be assumed when a motor-generating brain area is removed, thus emphasizing that the complexity of neural circuits can lead to initially counterintuitive results. Changes in swim-bout amplitude after ablation in the IO may be related to ataxia observed in mammals after IO lesions⁵³.

The tools developed in this study can be used to generate hypotheses about the roles of neurons (through whole-brain imaging and online model fitting) and to test them through targeted perturbation and reanalysis in the same experiment, in the same animal. We expect these capabilities to enable new types of experimental design.

Online content

Any methods, additional references, Nature Research reporting summaries, source data, statements of data availability and associated accession codes are available at <https://doi.org/10.1038/s41592-018-0221-x>.

Received: 17 February 2018; Accepted: 17 October 2018;

Published online: 30 November 2018

References

- Vogel, A. & Venugopalan, V. Mechanisms of pulsed laser ablation of biological tissues. *Chem. Rev.* **103**, 577–644 (2003).
- Deisseroth, K. Optogenetics: 10 years of microbial opsins in neuroscience. *Nat. Neurosci.* **18**, 1213–1225 (2015).
- Yang, W., Carrillo-Reid, L., Bando, Y., Peterka, D. S. & Yuste, R. Simultaneous two-photon imaging and two-photon optogenetics of cortical circuits in three dimensions. *eLife* **7**, e32671 (2018).
- Liu, X. et al. Optogenetic stimulation of a hippocampal engram activates fear memory recall. *Nature* **484**, 381–385 (2012).
- Chen, S., Chiu, C. N., McArthur, K. L., Fetcho, J. R. & Prober, D. A. TRP channel mediated neuronal activation and ablation in freely behaving zebrafish. *Nat. Methods* **13**, 147–150 (2016).
- Lee, J. H. et al. Global and local fMRI signals driven by neurons defined optogenetically by type and wiring. *Nature* **465**, 788–792 (2010).
- Boyden, E. S., Zhang, F., Bamberg, E., Nagel, G. & Deisseroth, K. Millisecond-timescale, genetically targeted optical control of neural activity. *Nat. Neurosci.* **8**, 1263–1268 (2005).
- Rickgauer, J. P., Deisseroth, K. & Tank, D. W. Simultaneous cellular-resolution optical perturbation and imaging of place cell firing fields. *Nat. Neurosci.* **17**, 1816–1824 (2014).
- Packer, A. M., Russell, L. E., Dalgleish, H. W. P. & Häusser, M. Simultaneous all-optical manipulation and recording of neural circuit activity with cellular resolution in vivo. *Nat. Methods* **12**, 140–146 (2015).
- Dal Maschio, M., Donovan, J. C., Helmbrecht, T. O. & Baier, H. Linking neurons to network function and behavior by two-photon holographic optogenetics and volumetric imaging. *Neuron* **94**, 774–789.e5 (2017).
- Carrillo-Reid, L., Han, S., Yang, W., Akrouh, A. & Yuste, R. Triggering visually-guided behavior by holographic activation of 1 pattern completion neurons in cortical ensembles 2 3. Preprint at <https://www.biorxiv.org/content/early/2018/08/17/394999> (2018).
- Chen, X. et al. Brain-wide organization of neuronal activity and convergent sensorimotor transformations in larval zebrafish. *Neuron* <https://doi.org/10.1016/j.neuron.2018.09.042> (2018).
- Portugues, R., Feierstein, C. E., Engert, F. & Orger, M. B. Whole-brain activity maps reveal stereotyped, distributed networks for visuomotor behavior. *Neuron* **81**, 1328–1343 (2014).
- Naumann, E. A. et al. From whole-brain data to functional circuit models: the zebrafish optomotor response. *Cell* **167**, 947–960.e20 (2016).
- Grosnick, L., Marshel, J. H. & Deisseroth, K. Closed-loop and activity-guided optogenetic control. *Neuron* **86**, 106–139 (2015).

16. Otchy, T. M. et al. Acute off-target effects of neural circuit manipulations. *Nature* **528**, 358–363 (2015).
17. Krakauer, J. W., Ghazanfar, A. A., Gomez-Marín, A., MacIver, M. A. & Poeppel, D. Neuroscience needs behavior: correcting a reductionist bias. *Neuron* **93**, 480–490 (2017).
18. Panier, T. et al. Fast functional imaging of multiple brain regions in intact zebrafish larvae using selective plane illumination microscopy. *Front. Neural Circuits* **7**, 65 (2013).
19. Ahrens, M. B., Orger, M. B., Robson, D. N., Li, J. M. & Keller, P. J. Whole-brain functional imaging at cellular resolution using light-sheet microscopy. *Nat. Methods* **10**, 413–420 (2013).
20. Vladimirov, N. et al. Light-sheet functional imaging in fictively behaving zebrafish. *Nat. Methods* **11**, 883–884 (2014).
21. Freeman, J. et al. Mapping brain activity at scale with cluster computing. *Nat. Methods* **11**, 941–950 (2014).
22. Alivisatos, A. P. et al. The brain activity map. *Science* **339**, 1284–1285 (2013).
23. Klapoetke, N. C. et al. Independent optical excitation of distinct neural populations. *Nat. Methods* **11**, 338–346 (2014).
24. Orger, M. B., Kampff, A. R., Severi, K. E., Bollmann, J. H. & Engert, F. Control of visually guided behavior by distinct populations of spinal projection neurons. *Nat. Neurosci.* **11**, 327–333 (2008).
25. Miri, A., Daie, K., Burdine, R. D., Aksay, E. & Tank, D. W. Regression-based identification of behavior-encoding neurons during large-scale optical imaging of neural activity at cellular resolution. *J. Neurophysiol.* **105**, 964–980 (2011).
26. Fang-Yen, C., Gabel, C. V., Samuel, A. D. T., Bargmann, C. I. & Avery, L. Laser microsurgery in *Caenorhabditis elegans*. *Methods Cell Biol.* **107**, 177–206 (2012).
27. Nishimura, N. et al. Targeted insult to subsurface cortical blood vessels using ultrashort laser pulses: three models of stroke. *Nat. Methods* **3**, 99–108 (2006).
28. Liu, K. S. & Fetcho, J. R. Laser ablations reveal functional relationships of segmental hindbrain neurons in zebrafish. *Neuron* **23**, 325–335 (1999).
29. Mendelson, B. Development of reticulospinal neurons of the zebrafish. II. Early axonal outgrowth and cell body position. *J. Comp. Neurol.* **251**, 172–184 (1986).
30. McLean, D. L. & Fetcho, J. R. Ontogeny and innervation patterns of dopaminergic, noradrenergic, and serotonergic neurons in larval zebrafish. *J. Comp. Neurol.* **480**, 38–56 (2004).
31. Randlett, O. et al. Whole-brain activity mapping onto a zebrafish brain atlas. *Nat. Methods* **12**, 1039–1046 (2015).
32. Thiele, T. R., Donovan, J. C. & Baier, H. Descending control of swim posture by a midbrain nucleus in zebrafish. *Neuron* **83**, 679–691 (2014).
33. Roeser, T. & Baier, H. Visuomotor behaviors in larval zebrafish after GFP-guided laser ablation of the optic tectum. *J. Neurosci.* **23**, 3726–3734 (2003).
34. Lemon, W. C. et al. Whole-central nervous system functional imaging in larval *Drosophila*. *Nat. Commun.* **6**, 7924 (2015).
35. Tomer, R., Khairy, K., Amat, F. & Keller, P. J. Quantitative high-speed imaging of entire developing embryos with simultaneous multiview light-sheet microscopy. *Nat. Methods* **9**, 755–763 (2012).
36. Royer, L. A. et al. Adaptive light-sheet microscopy for long-term, high-resolution imaging in living organisms. *Nat. Biotechnol.* **34**, 1267–1278 (2016).
37. Dana, H. et al. Sensitive red protein calcium indicators for imaging neural activity. *eLife* **5**, 413–420 (2016).
38. Kawashima, T., Zwart, M. F., Yang, C.-T., Mensh, B. D. & Ahrens, M. B. The serotonergic system tracks the outcomes of actions to mediate short-term motor learning. *Cell* **167**, 933–946.e20 (2016).
39. Sugihara, I., Lang, E. J. & Llinás, R. Serotonin modulation of inferior olivary oscillations and synchronicity: a multiple-electrode study in the rat cerebellum. *Eur. J. Neurosci.* **7**, 521–534 (1995).
40. Ito, M. Long-term depression as a memory process in the cerebellum. *Neurosci. Res.* **3**, 531–539 (1986).
41. Bae, Y.-K. et al. Anatomy of zebrafish cerebellum and screen for mutations affecting its development. *Dev. Biol.* **330**, 406–426 (2009).
42. Bouchard, M. B. et al. Swept confocally-aligned planar excitation (SCAPE) microscopy for high speed volumetric imaging of behaving organisms. *Nat. Photonics* **9**, 113–119 (2015).
43. Tomer, R. et al. SPED light sheet microscopy: fast mapping of biological system structure and function. *Cell* **163**, 1796–1806 (2015).
44. Quirin, S. et al. Calcium imaging of neural circuits with extended depth-of-field light-sheet microscopy. *Opt. Lett.* **41**, 855–858 (2016).
45. Fahrbach, F. O., Voigt, F. F., Schmid, B., Helmchen, F. & Huisken, J. Rapid 3D light-sheet microscopy with a tunable lens. *Opt. Express* **21**, 21010–21026 (2013).
46. Patterson, G. H. & Lippincott-Schwartz, J. A photoactivatable GFP for selective photolabeling of proteins and cells. *Science* **297**, 1873–1877 (2002).
47. Ahrens, M. B. et al. Brain-wide neuronal dynamics during motor adaptation in zebrafish. *Nature* **485**, 471–477 (2012).
48. Motta-Mena, L. B. et al. An optogenetic gene expression system with rapid activation and deactivation kinetics. *Nat. Chem. Biol.* **10**, 196–202 (2014).
49. Singh, C., Oikonomou, G. & Prober, D. A. Norepinephrine is required to promote wakefulness and for hypocretin-induced arousal in zebrafish. *eLife* **4**, e07000 (2015).
50. Lovett-Barron, M. et al. Ancestral circuits for the coordinated modulation of brain state. *Cell* **171**, 1411–1423.e17 (2017).
51. Severi, K. E. et al. Neural control and modulation of swimming speed in the larval zebrafish. *Neuron* **83**, 692–707 (2014).
52. Wang, W.-C. & McLean, D. L. Selective responses to tonic descending commands by temporal summation in a spinal motor pool. *Neuron* **83**, 708–721 (2014).
53. Horn, K. M., Deep, A. & Gibson, A. R. Progressive limb ataxia following inferior olive lesions. *J. Physiol. (Lond.)* **591**, 5475–5489 (2013).

Acknowledgements

We thank F. Engert, N. Li, A. Bolton, A. Hantman, and B. Mensh for comments on the manuscript; V. Goncharov, D. Flickinger, C. McRaven, and Janelia Experimental Technology for help with microscopy design and construction; D. Flickinger for helpful discussions on ETL-based remote focusing; M. Zwart for discussions on optogenetics; T. Kawashima for technical assistance; M. Coleman, A. Chiu, and F. Angstadt for assistance with coding; S. Sawtelle for discussions and ETL driver construction; D. Leuenberger and C. Grätzel at Optotune for discussions; J. Cox, B. Foster, J. Rouchard, and C. McGlynn for fish husbandry; D. Bennet for assistance with Thunder code; K. Branson, S. Romani, M. Rubinov, and A. Porrello for helpful discussions; G. Ceric, K. Carlile, and R. Lines for assistance with the high-performance computer cluster; and S.-I. Higashijima (NIBB, Japan) for providing the fish lines labeling gad1b- and vGlut2a-positive neurons. This work was supported by the Howard Hughes Medical Institute (M.K., P.J.K., and M.B.A.); by the Simons Foundation–Simons Collaboration on the Global Brain Research Awards 325171 and 542943SPI (J.F. and M.B.A.); and by MDC Berlin (S.P.).

Author contributions

N.V., C.W., P.J.K., and M.B.A. conceived the project. N.V. and M.B.A. designed and built the laser ablation system for Zebrascopes. N.V. created the software for brain mapping. C.W. and P.J.K. designed and built the Opto-SiMView microscope for concurrent 3D imaging and 3D optical manipulation. N.V., C.W. and B.H. created the software for brain perturbation. N.V. performed the ablation-based experiments in Figs. 1–4; C.W. and B.H. performed the optogenetics-based experiments in Figs. 5 and 6; M.T. and M.K. performed the ablation experiments in Supplementary Fig. 1c; A.P., N.V., and M.K. performed the ablation experiments in Fig. 1g,h. Y.M. contributed to cross-modal fish brain registration. J.F., J.D.W., and S.P. contributed to software. C.-T.Y. generated the *Tg(elavl3:jRGECO1b)* and *Tg(elavl3:CoChR-eGFP)* lines. P.J.K. and M.B.A. supervised the work. N.V., C.W., P.J.K. and M.B.A. wrote the paper.

Competing interests

The authors declare no competing interests.

Additional information

Supplementary information is available for this paper at <https://doi.org/10.1038/s41592-018-0221-x>.

Reprints and permissions information is available at www.nature.com/reprints.

Correspondence and requests for materials should be addressed to N.V. or P.J.K. or M.B.A.

Publisher's note: Springer Nature remains neutral with regard to jurisdictional claims in published maps and institutional affiliations.

© The Author(s), under exclusive licence to Springer Nature America, Inc. 2018

Methods

Design of microscope for laser ablation and light-sheet imaging during behavior. The light-sheet microscope, behavior setup, and two-photon ablation arm were based on a previously reported setup, Zebrascopes²⁰, to which we coupled a steered femtosecond infrared laser described in the next paragraph. Briefly, the detection arm consisted of a water-dipping detection objective (16×/0.8 NA, Nikon) mounted vertically on a piezo stage, a tube lens, and an sCMOS camera (Orca Flash 4.0, Hamamatsu). The *z* position of the objective was controlled by a piezo stage (Physik Instrumente). The detection arm was further equipped with a band-pass filter (525/50 nm, Semrock) for separating GCaMP-fluorescence light from scattered 488-nm-laser light. Each of the two light-sheet illumination arms consisted of an air illumination objective (4×/0.28 NA, Olympus) mounted horizontally on a piezo stage, a tube lens, an *f*- θ lens and a pair of galvanometer scanners. The scan mirrors and *f*- θ lens scanned the collimated laser beam (488 nm) laterally and along the *z* axis of the image space. The 488-nm laser in the side excitation arm was rapidly (electronically) turned off every time the laser was scanned over the eye of the fish, thus avoiding direct stimulation of the retina. A detailed list of hardware is shown in Supplementary Table 1. We acquired 2,048 × 1,024 pixel images, over 41 *z* locations spaced 5 μ m apart, at a 1.8-Hz volumetric-imaging rate. The acquisition settings for the light-sheet imaging data shown in Supplementary Video 3 were identical, except for the stack size and temporal resolution: a single plane was imaged at a rate of 50 images/s.

Two-photon excitation optical arm. The focus spot of a femtosecond titanium-sapphire laser (Coherent Chameleon Ultra II, tuned at 930 nm) was steered along the *xy* directions of the imaging plane by a pair of galvanometric mirrors conjugated to the back focal plane of the imaging objective (16×/0.8 NA, Nikon) through an expanding telescope, which consisted of a custom-made *f*- θ lens (*f* = 33 mm) and a Nikon tube lens (*f* = 200 mm). *z* positioning of two-photon excitation spots was performed by the imaging-objective piezo stage. Laser power for two-photon excitation was modulated with an electronically controlled Pockels cell (Conoptics).

Optical alignment between imaging and ablation arms. To match the imaging plane with a two-photon excitation plane in the axial direction, we used two-photon excitation of a fluorescein sodium salt in water solution with simultaneous imaging through the detection objective. We then adjusted the collimation of the two-photon beam entering the detection objective so that the size of the two-photon excitation spot seen on the detection camera was minimized, thus ensuring that the axial position of the two-photon excitation laser focus matched the imaging-plane position. The mapping of the command voltage for the *xy* galvanometric mirrors to camera pixel coordinates was performed with the fluorescein solution by creating excitation spots in a 2D grid across the field of view and applying spline interpolation in a custom LabView program.

Behavior setup and experiments. All experiments were conducted according to protocols approved by the Institutional Animal Care and Use Committee of the Howard Hughes Medical Institute, Janelia Research Campus. Larval zebrafish were paralyzed through a brief immersion in 1 mg/ml α -bungarotoxin (Invitrogen) dissolved in 'external' solution (134 mM NaCl, 2.9 mM KCl, 2.1 mM CaCl₂, 1.2 mM MgCl₂, 10 mM HEPES, and 10 mM glucose, pH 7.8; 290 mOsm) for 30 s. Once paralyzed, the fish were embedded in 2% low-melting point agarose (Sigma-Aldrich) in a custom-made chamber²⁰. The imaging chamber was then filled with a solution containing Instant Ocean salt from Carolina Biological Supply Company (65 mg/L Instant Ocean, 30 mg/L sodium bicarbonate), the same medium in which the fish were raised. After the chamber was transported to the experimental apparatus, electrical recordings from the motor neuron axons in the tail were made according to previously described techniques^{47,54}. Briefly, extracellular recordings were made with fire-polished glass pipettes with a tip diameter of approximately 40 μ m, with an Axon Multiclamp 700B amplifier in current clamp setting. Electrodes were advanced with manual micromanipulators until they touched the dorsal part of the intact tail, after which gentle suction was applied to seal them to the tissue and record signals from the ventral root (intended motor output of the paralyzed fish). Electrodes were filled with external solution. Signals were sampled at 6 kHz and band-pass filtered with a low-pass cutoff at 1.4 kHz and a high-pass cutoff at 100 Hz. To identify swim bouts, we further processed the signals by taking the local s.d. in a sliding 10-ms window, after which a simple thresholding operation could be used to identify swim onset and offset, and the occurrence of 'fictive fail flicks'. Signals were recorded, and visual stimuli were presented with custom software written in C# (Microsoft). Fish with erratic behavior (such as inconsistent response to the stimulus, owing to long periods of behavioral silence) or noisy fictive signals (potentially due to poor electrical contact between the electrode and the skin above the motor nerve) were excluded (approximately 25% of all tested fish). Fish were imaged in water at a temperature of 22 °C.

Visual-stimulus delivery. A fish holder was mounted on the transparent acrylic bottom section of the chamber, thus simplifying the process of removing the agarose surrounding the animal. A diffusive plastic screen was attached to the bottom of the chamber from the outside, to allow for image projections from below

with a miniature projector producing red monochromatic images. The visual stimulus was generated with a Sony Pico Mobile Projector (MPCL1) connected to the behavior-acquisition and control computer.

Optomotor response. A red/black grating with a spatial period of ~1.2 cm was presented to the fish, alternating between periods of backward stimulus (head to tail, 5.5 s), pauses (1.1 s), and forward (tail to head, 14.5 s) motion. The timing of the stimulus was synchronized with the imaging. The speed of each stimulus was randomly chosen at each trial from 0, -0.12, -0.24, and -0.48 cm/s (backward), or 0, 0.12, 0.24, and 0.48 cm/s (forward). During the forward stimulus, vigorous fictive swimming was typically observed (Pearson's $r = 0.31 \pm 0.12$ between the F stimulus and swimming, mean \pm s.d.). During backward or zero motion, there was little or no swimming ($r = -0.13 \pm 0.09$ between the B stimulus and swimming). Because the OMR experiments were open loop, fictive swimming of the fish did not affect the stimulus motion. We performed OMR experiments before and after ablation, both with imaging and without imaging, in each fish. For the quantification of behavior in Fig. 3, we used behavioral data from the session without imaging. Postablation behavior was assessed 20–30 min after ablation.

Transgenic zebrafish. The transgenic zebrafish larvae used in this study were in the *nacre* background⁵⁵. We used previously published transgenic zebrafish lines expressing GCaMP6f either in the cytosol *Tg(elavl3:GCaMP6f)*⁶¹ or the nucleus *Tg(elavl3:H2B-GCaMP6f)*⁶⁷ (refs. ^{21,44,56}); the lines *Tg(elavl3:CoChR-eGFP)* and *Tg(elavl3:jRGECO1b)* were generated as described earlier with Tol2 and an *elavl3* sequence²¹. For imaging of double-transgenic fish, we used *TgBAC(gad1b:loxP-RFP-loxP-GFP)*, as described previously⁵⁷, and *TgBAC(slc17a6b:loxP-DsRed-loxP-GFP)*, as described previously^{57,58}, in the absence of Cre-mediated recombination; these genotypes are referred to as *Tg(gad1b:RFP)* and *Tg(vGlut2a:dsRed)*, respectively (lines provided by S.-I. Higashijima, NIBB, Japan). The larvae were reared under 14:10 light/dark cycles according to the standard protocol at 28.5 °C, in a solution containing Instant Ocean salt from Carolina Biological Supply Company (65 mg/L Instant Ocean and 30 mg/L sodium bicarbonate).

Data storage and processing infrastructure. A single imaging session in our microscope for light-sheet imaging during behavior typically lasted 11 min and generated 197 Gb imaging data (1,200 time points, 164 Mb/volume stack, each stack 1,024 × 2,048 × 41 voxels, 16-bit images), acquired at a rate of 1.8 volumes/s. This rate of data acquisition (2.5 GB/s) allowed us to log data directly to a cluster storage system via a 10-GB Ethernet connection. To quickly compute brain-wide functional maps, we typically used 20 nodes of the Janelia cluster running Spark, a process requiring approximately 10 min of computing time (Supplementary Table 2). The cluster nodes ran Scientific Linux 7.3, and each node contained 16 cores (2.7 GHz Intel Sandy Bridge, E5-2680), 128 GB RAM, 10 Gb Ethernet, and single hard drives. Computation was parallelized with the Thunder/Spark framework²¹.

Computation of the brain activity maps. We computed functional maps from the time-varying GCaMP6f-intensity signal in neurons with pixel-wise linear regression^{21,25} with a 'minimal model' based on three regressors in which neural activity was determined by linear combinations of three variables: the speed of forward-stimulus motion (g_1), the speed of backward-stimulus motion (g_2), and the fictive-swim signal (g_3):

$$G(t) = [g_1(t), g_2(t), g_3(t)]$$

$$X(t) = G\beta + \epsilon$$

Here $t = 1 \dots T$ is the time index, $G(t)$ is a $T \times 3$ matrix of regressors, and $X(t) \stackrel{\text{def}}{=} \frac{F(t) - \langle F \rangle}{(\langle F \rangle - 100) + 20}$ is the time series of relative fluorescence variation of each pixel over time ($\Delta F/F$), where $F(t)$ is the absolute pixel fluorescence, and $\langle F \rangle$ is the tenth percentile of F in a sliding window of 100 time points, equivalent to a period of 55 s (i.e., $\langle F(t) \rangle$ is the tenth percentile of $F(t - 50) \dots F(t + 49)$), with offset factors of 100 and 20 to account for the camera noise (which gives a readout value of approximately 100 in darkness) and to avoid division by zero, respectively. For each voxel in the data, the linear-regression algorithm performs a least-squares estimate of regression coefficients $\beta = (\beta_1, \beta_2, \beta_3)$ that predict $X(t)$ with minimum residual error ϵ . Both stimuli and behavior were convolved with an estimated calcium-impulse-response function of GCaMP6 modeled as an exponential-decay kernel with a decay time of 1.5 s to mimic the neuronal response to a spike, and normalized by their s.d.

The relative weights of regressors ('weights' throughout the paper) were defined from the regression coefficients and the coefficient of determination R^2 by the formula

$$w_i = (\beta_i R^2)^{0.5}, \beta_i \geq 0, i = 1, 2, 3$$

Multiplication by the coefficient of determination R^2 decreased the noise, and in the extreme case of a 'non-fit' set the relative weight to near zero; the gamma correction (power 0.5) highlights neurons that otherwise would appear very dim. The weights w_i were then converted into 8-bit grayscale values and then combined into color-coded images (stacks) to represent the functional maps.

The brain-activity trajectories in the areas covered by the masks (Supplementary Fig. 3c) were calculated voxel-wise with the ninety-fifth-percentile

$\Delta F(t)/F_0(t)$ of all voxels within the masked region at a given time point and subsequent averaging across the voxels; thus, the trajectories represented the most active 5% of activity in each of the included brain areas.

The Python code of the main data processing pipeline is available at <https://github.com/optofish-paper/> and uses the Thunder package²¹, which can be downloaded at <http://thunder-project.org/>. Owing to the large size of the original data and cluster requirement, the example code uses downsampled data as a test, and it can be run on a desktop computer.

Selection of ablation targets. The resulting RGB TIFF files were opened in ImageJ/FIJI for visual inspection, and ablation targets were manually selected with the custom-written FIJI plugin, which recorded the x, y, z positions of the targets and converted them into a text script that the microscope control software could read.

Ablation protocol. To ablate individual neurons, we used two-photon-laser plasma ablation that was based on published protocols and optimized to act on sub-single-neuron spatial scales^{1,26}. We used a high-power laser (500 mW, measured after the objective, using a Coherent Chameleon Ultra II laser) at 930-nm wavelength with a very short exposure time (1–2 ms for neurons 0–100 μm from the dorsal brain surface, up to 3–4 ms in ventral areas 150–200 μm deep). The time interval between successive ablation points was chosen to be 5 s to allow for the heat released by cell ablation to dissipate and minimize unintended brain damage. The choice of short exposure and long interablation interval allowed us to avoid cavitation (water-vapor bubbles) in the brain tissue. In our hands, longer exposure times tended to produce off-target effects, whereby such bubbles occurred, and single-neuron resolution was lost; restricting the exposure time to 1–4 ms avoided such effects and produced sub-neuron-scale cell damage.

In the behavioral tests, the OMR assay was started 20 min before ablation and was followed by an ablation session lasting 5–10 min, then more OMR behavior trials for another 30–40 min after ablation.

Ablation accuracy was optimized by decreasing sample drift in the x, y and z directions. This process included minimization of the thermal drift of microscope components via thermal isolation of posts and a sample stage with foam-rubber insulation, and registration of a brain image taken directly before ablation, to compensate for residual drift between the imaging session and ablation onset. This residual drift was typically approximately 5–7 μm along the rostro-caudal axis of the fish and less than 2.5 μm in the z direction, and was fully compensated by registration. We used xyz-translation registration for most experiments and also implemented a Python interface for the FIJI Multiview-Reconstruction plugin⁵⁹, which allows for rigid-body registration (translation and rotation) and improves the accuracy and speed of the ablation-coordinate correction.

The average numbers of cells targeted in each case were, across fish: fc-nMLF, 44 ± 22 cells per fish (eight fish); fc-IO, 112 ± 53 cells per fish (eight fish); fc-RoL1, 104 ± 52 cells per fish (ten fish); fc-preT, 155 ± 45 cells per fish (nine fish); fc-DHB, 160 ± 69 cells per fish (12 fish) per brain area (average \pm s.d.); and control in optic tectum, 150 ± 0 cells per fish (four fish).

For controls, ablations in the optic tectum were carried out (Fig. 2h, brain-wide activity, 150 neurons per brain), as well as of randomly chosen neurons in the hindbrain (Fig. 3, behavior tests, 'rand' bars, 150 neurons per brain). To control for any effects of fish handling alone on behavior, 'sham' ablations were also carried out (Fig. 3, behavior tests, 'sham' bars), in which fish were handled and imaged as usual, but no ablation was made.

Statistical analysis of the effects of lesions on behavior. To statistically evaluate⁶⁰ the effects of the ablations on individual measures of behavior, as shown in Fig. 3, we took into account that we used multiple behavioral measures, quantified as $(x_{\text{post}} - x_{\text{pre}})/(x_{\text{post}} + x_{\text{pre}})$ of various behavior metrics x (where x is the swim duration during forward motion, the swim duration during backward motion, and so forth). We first determined that the ablations had an effect on behavior with multivariate ANOVA (across all brain areas at once; with brain area and a vector of all behavioral measures, $P = 0.0013$). To evaluate the effects of lesions in individual areas on the six behavioral measures, we controlled the FWER⁶¹ per brain area to be 0.05, i.e., an estimated 5% chance of any behavioral measure being falsely counted as significant. For each (brain area, behavioral measure) test, we used two-tailed t tests (normality was assessed with a $P = 0.05$ cutoff with a Shapiro–Wilk test) or Wilcoxon signed-rank tests (if a Shapiro–Wilk test rejected the null hypothesis that the data are normally distributed; less than 10% of tests) and included a statistical correction factor to achieve this FWER per brain area, calculated as follows. We shuffled, per fish, pre versus post time-averaged behavior 20,000 times (i.e., a 0.5 probability of switching the pre and post labels for the data, independently for each fish but, by switching the entire data time series, coordinated across behavioral measures), and required, for each brain area, that the ablation had any statistically significant effect at most one-twentieth of the time. (This procedure is conceptually equivalent to performing, per brain area, the set of experiments 20 times, and requiring that there can be a false positive at most once.) The average correction factor per area was 3.9, a value smaller than the number of behavioral measures because some of the behavioral measures are correlated (for example, swim frequency during the forward stimulus may be correlated with

swim frequency during the backward stimulus); thus, the cutoff for statistical significance for each lesioned area was set at $P < 0.05/(\text{correction factor for that area})$.

Statistical analysis of the effects of lesions on activity across the brain. For evaluating the significance of the effects of lesions on the s.d. of activity in other brain areas, as shown in Fig. 4, we first assessed statistical significance with n -way ANOVA to test whether lesions across brain areas led to changes in activity in the measured regions of interest ($P < 0.0001$ both for ablation site and region of interest), and next again used two-tailed t tests (after a Shapiro–Wilk test for normality did not reject the null hypothesis that the data were normally distributed, with a $P = 0.05$ cutoff) or Wilcoxon signed-rank tests (after the Shapiro–Wilk test rejected the null hypothesis that the data were normally distributed) with a correction based on a similar shuffle procedure to again control the FWER per lesioned brain area to be 0.05. For the control ablation of randomly selected cells in the tectum, each shuffle consisted of randomly switching the entire pre- and postlesion activity traces (with a probability of 0.5 per fish, independently for each fish), and requiring that any effect on any region of interest was significant in at most 1/20 shuffles, thus yielding an average correction factor of 5.5, reflecting dependencies among activity in multiple regions of interest; significance was therefore set to $P < 0.05/(\text{correction factor for brain area})$.

M cell-ablation experiments and statistical analysis. For examining the effects of cell ablations on the escape response, we used the naturally paralyzed relaxed mutant fish⁶² expressing nuclear *GCaMP6f* under control of the neuronal *elavl3* promoter. The use of this fish obviated the need to use cholinergic blockers to induce paralysis during imaging and fictive-behavior experiments. Consequently, in this fish, we were able to monitor the output of the escape circuit by recording EMGs from trunk muscles. To elicit escape responses while imaging calcium activity in the brain, we delivered electrical shocks to the dorsal portion of the tail fin with a concentric bipolar tungsten electrode (Microprobes). First, before imaging, a stimulus threshold was determined as the lowest intensity at which the stimulus unfailingly produced a short-latency (<10 ms) escape response for three or four stimuli delivered at greater than 2 min intervals. Then, for the imaging session, the stimulus threshold was kept at 1.5 times the threshold value in an attempt to ensure the stability of escape responses for the entire time period over which the experiment occurred (approximately 1 h). In the first session of stimulation, stimuli were delivered regularly at 1-min intervals for approximately 10 min while the brain was imaged with the light-sheet microscope at approximately two volumes per second (40 planes with 5 μm between the planes). Then, with the collected images, registration-based activity maps of the brain were computed quickly (within approximately 10 min) by parallelizing image-processing computations over the Janelia computing cluster. Functional maps were computed as described in Methods, with linear regression against behavior and stimulus. The resulting functional maps served as a guide to identify neurons that were either correlated or uncorrelated to the escape responses elicited by the shock. In one set of experiments (six fish), the M cell—which is responsible for the large initial C bend of the escape response⁶³—ipsilateral to the side of the tail stimulation was ablated, whereas in a different set of experiments (five fish), seven or eight neurons that did not appear in the functional maps but that were in the vicinity of the M cell (within $\sim 20 \mu\text{m}$) were ablated. The parameters related to ablation (such as laser power and pulse duration) were similar to those described above. After ablation of either the M cell or other neurons, we waited for at least 20 min to allow for recovery from a possible change in brain state in response to the ablations. At the end of this waiting period, we carried out a second 10-min imaging and stimulation session wherein the imaging and stimulation parameters were kept identical to those used before the ablation.

The effects of ablation were assessed by comparison of the onset latencies of shock-elicited responses before and after the ablation. Onset latencies were measured manually for the first response within the 100-ms EMG trace after a stimulus, after each such trace was presented to the experimenter by a MATLAB (Mathworks) script in random stimulus and without displaying any information indicating whether the response occurred before or after cell ablations. Thus, when measuring onset latencies, the experimenter was not biased by expectations concerning the effects of ablation on response latency. If a response was not seen within the first 100 ms after a stimulus, then that stimulus trial was deemed as not having elicited a response. For assessing significance, the latencies for each fish were averaged across stimulus trials for each of the conditions, before and after ablation of the M cell ($n = 6$, before and after ablation of other cells ($n = 5$)). Because the data points were not normally distributed, we carried out paired nonparametric Wilcoxon tests to compare latencies before and after ablation and found that they were significantly delayed after ablation of the M cell ($P = 0.027$) but not other cells ($P = 0.345$). Thus, our results showed that ablation of M cells, but not other cells, results in a significant delay in shock-elicited response latencies.

Electrophysiological verification of the effects of two-photon laser ablation.

To verify the effects of the laser pulse on neural activity, spikes were recorded extracellularly from nMLF neurons (four MeLr and one MeLc neurons in five fish) in *Tg(elavl3:GCaMP6f)* fish in which spinal projection neurons were sparsely

backfilled with 20% fluorescent dye (Texas Red dextran, MW 10,000, Thermo Fisher Scientific). A pipette was pulled from a borosilicate glass capillary (BF150-86-10, Sutter) with a pipette puller (P-1000, Sutter) and filled with external solution containing 0.02% fluorescent dye (Alexa Fluor 680 dextran, MW 10,000, Thermo Fisher Scientific). The pipette resistance was between 5 and 10 M Ω . Loose-patch recordings were made with an amplifier (EPC 10 USB Quadro, Heka) filtered at 10 kHz and digitized at 6 kHz with a data-acquisition board (PXIe-1078, National Instruments) with software custom written in C# (Microsoft).

Estimation of two-photon excitation focus volume. We observed that in most cases, the effects of two-photon ablation were confined to the targeted neuron. The neurons expressing GCaMP6f in the nucleus became very bright, with a central small black spot less than 1 μm in diameter, presumably because of photodamage of GCaMP6f at the excitation volume (Fig. 1e, right). To verify that this result was consistent with theoretical estimates of the excitation region, we estimated the volume of two-photon excitation V_{ex} from the two-photon PSF² radii^{64,65},

$$\omega_{x,y} = \frac{0.325\lambda}{\sqrt{2}NA^{0.91}} = 0.26 [\mu\text{m}]$$

$$\omega_z = \frac{0.532\lambda}{\sqrt{2}(n - \sqrt{n^2 - NA^2})} = 1.31 [\mu\text{m}]$$

$$V_{\text{ex}} = \pi^{3/2} (\omega_{x,y})^2 \omega_z = 0.5 [\mu\text{m}^3]$$

This volume is less than 1% of an estimated neuronal nucleus volume in zebrafish $\frac{4}{3}\pi 2.5^3 = 65 \mu\text{m}^3$, thus, under ideal conditions, confining the two-photon ablation within subcellular dimensions.

Postablation imaging and behavior recording. After testing postablation behavior continuously for 30–40 min, we performed a new imaging session to map the changes in brain activity. The parameters of the postablation imaging were identical to those of preablation imaging, described above.

Nonrigid registration to Z-Brain. To register fish brains to the Z-Brain template, we used ANTs software⁶⁶ (<http://stnava.github.io/ANTs/>) and a combination of rigid and nonrigid (SyN) transformations. The brains were downsampled to 5 μm isotropic resolution before registration to speed up registration, but the resulting computed subpixel transformations were applied to full-resolution functional maps (1,024 \times 2,048 \times 41 pixels) before averaging across fish (Fig. 2c–h). Python wrapper code for ANTs registration and postprocessing is available online (<https://github.com/optofish-paper/>).

Design of Opto-SiMView multiview microscope with an ETL-based 3D-manipulation arm.

System overview. The microscope consists of three laser light sources and five optical arms, including two arms for laser light-sheet illumination, two arms for wide-field fluorescence imaging and one arm for 3D point-scanning optical manipulation with digitally controlled optical power. Two of the three light sources are multilaser systems for laser light-sheet illumination with one-photon excitation, including a SOLE-6 and a SOLE-3 system (Omicron Laserage). The third light source is a pulsed titanium-sapphire laser (Chameleon Ultra II, Coherent) for two-photon optical manipulation. The optical manipulation arm is coupled into the microscope via one of the detection arms. The SOLE-6 and SOLE-3 units each have two exit ports at which the multilaser beams (405 nm, 454 nm, 488 nm, 561 nm, and 594 nm) are coupled to the two light-sheet illumination arms with two single-mode fibers. Each illumination arm consists of a shutter (VS14S2ZM1-100, Vincent Associates), an illumination filter wheel with controller (96A351 and MAC6000, Ludl), a dual-axis galvanometer scanner with 6-mm mirrors (6215HSM40B scanner with 673XX dual-axis class 1 integrating servo driver amplifier, Cambridge Technology) mounted on an x-y- θ multiaxis stage (XYR1, Thorlabs), a custom telecentric f - θ lens with 80-mm focal length (66-s80-30T, Special Optics), and a custom water-dipping illumination objective (54-12.5-31, Special Optics) mounted on a linear-translation piezo stage with controller (P-625.1CD and E-665, Physik Instrumente). The x mirror of the galvanometer scanner (responsible for lateral displacement of the scanned light sheet) is conjugated to the back aperture of illumination objective.

Each detection arm consists of a detection filter wheel (96A354, Ludl), operated with the same controllers as those used for the illumination filter wheels, with multiple band-pass and long-pass filters (Semrock), a tube lens with a focal length of 200 mm (MXA22018, Nikon), a 16 \times /0.8 water-dipping detection objective (CFI75 LWD 16 \times W, NA 0.8, Nikon) mounted on a linear-translation piezo stage with controller (P-625.1CD and E-665, Physik Instrumente), and an sCMOS camera (Orca Flash 4.0 v2, Hamamatsu).

The infrared light beam from the femtosecond pulsed titanium-sapphire laser passes through a Pockels cell with controller (350-80 and 302RM, Conoptics), a telescope lens pair (65-438 and 47-380, Edmund Optics), and an ETL (EL-10-30-CI-NIR-LD, Optotune) operated by a custom-built driver (described below), which enables controlling the z position of the laser focus independently of the voltage setting applied to the piezo controlling the position of the detection objective. For controlling the x and y positions of the laser focus, we used a pair

of galvanometer scanners with 10-mm beryllium mirrors (6220H, Cambridge Technology) after the ETL. The ETL is conjugated to the x mirror with a pair of relay lenses (49-361-INK, Edmund Optics), and the x mirror is conjugated to the y mirror with two custom telecentric f - θ lenses with 80-mm focal length (66-s80-30T, Special Optics). A third f - θ lens of the same type and a VIS-NIR achromatic lens (49-391-INK, Edmund) are used to conjugate the y mirror to the back aperture of the Nikon detection objective and expand the beam 1.875-fold to better fill the objective aperture. The beam is coupled into the detection arm with a customized dichroic mirror with $\lambda/10$ flatness (T680 spxr, 5-mm thickness, Chroma). Conjugation of the ETL to the back aperture of the objective is critical to ensure a linear change in focal shift in sample space as a function of the control current delivered to the ETL. The ETL focusing z range in sample space depends on the beam radius at the ETL location (and thus on the effective numerical aperture in sample space). The Opto-SiMView described here uses a 6.7-diopter ETL, providing a z range of 350–400 μm (dashed gray line in Fig. 5c). A 20-diopter ETL (such as Optotune model EL-16-40-TC-VIS-5D-C) can be used to increase the z range up to 1,200 μm . We further measured a light transmission rate of 80% of the optical manipulation arm (from the exit port of the Pockels cell to the back aperture of the objective). A detailed list of microscope components is presented in Supplementary Table 3.

Custom ETL driver. We developed a custom ETL driver (Supplementary Data 2) to compensate for several fundamental shortcomings of the standard driver shipped with the ETL. The primary issue with the standard controller model is the low maximum rate (≤ 100 Hz) at which commands are sent to the ETL. In focal-power mode with sensor control (i.e., the mode that supports ETL temperature readout and feedback/compensation), the native control software processes the signal and sends new focal power settings to the ETL driver once every 50 ms. The current command on the driver then requires another 100 μs to be processed. In addition, sending a fast stream of commands starves the main loop in the firmware of the ETL driver, which in turn makes the timing of current commands sent to the lens unpredictable. Overall, these performance bottlenecks severely limit the smoothness of ETL focus changes and the speed at which the system can operate. During high-speed volumetric imaging, the piezo stages move at a speed of 0.83 $\mu\text{m}/\text{ms}$ and require a stability of the manipulation focus of approximately $\pm 1 \mu\text{m}$ for spatially precise optogenetic control. The standard ETL driver is thus much too slow for generating the smooth ETL-mediated focus shift needed to keep up with the motion of the piezo.

Our high-speed, high-precision custom ETL driver provides a unipolar voltage-controlled linear current directly to the Optotune electric tunable lens coil. The custom driver consists of three main components: (i) a voltage-current converter, (ii) an I²C communication board (USB-8451, National Instruments), and (iii) a small printed circuit board. The driver is connected to the Optotune ETL via a Hirose cable and to the microscope-control computer running our custom LabVIEW control software via USB. The driver furthermore provides a buffered current output monitor.

The voltage-current converter continuously converts the 0- to 5-V analog signal to a current with a transfer function of 10 V/A and a conversion rate of up to 500 kHz. This converter is connected to pins 1 and 2 of the Hirose port of the ETL. The analog voltage signal is provided by a National Instruments PXI-6733 card in the microscope's real-time controller, which generates a 16-bit analog output at a rate of 50 kHz. Overall, our microscope-control framework and custom driver can thus generate a current with 0.0075 mA precision at an update rate of 50 kHz. The maximum acceptable input current to the ETL is 290 mA. In our optical design, an ETL current of 250 mA corresponds to a shift of 380 μm in focus position. Thus a 1- μm focus shift is achieved by a 0.66 mA current change (corresponding to a 6.6-mV voltage change).

The printed circuit board provides pull-ups for I²C communication (required for interacting with the temperature sensor of the ETL) and a voltage regulator to convert the 5 V supplied by the USB-8451 board to the 3.3 V required by the ETL. Power and I²C are connected to the ETL via pins 3, 4, 5, and 6 of the Hirose port.

Our LabVIEW control software reads out the temperature of the ETL at a rate of 10 Hz. The resolution of the temperature sensor is 0.125 $^{\circ}\text{C}$.

Calibration procedure and control of the ETL-based 3D-manipulation arm in Opto-SiMView.

Calibration procedure of the ETL-based 3D-manipulation arm. 3D calibration is performed with a fluorescent target in the reference frame of detection arm 1 (with camera 1 as the primary detector) and consists of two main steps: the calibration of the ETL (positioning the focus along the z axis) and the calibration of the galvanometer scanner (positioning the focus along the x and y axes). The target consists of a thin-walled Teflon tube of 2.5-mm diameter, which is filled with 500 $\mu\text{g}/\text{l}$ fluorescein dye in distilled water.

In the first step, a set of current values is sequentially applied to the ETL (by controlling input voltage levels to the ETL driver, sampling the voltage range 0–2.5 V in ten steps), and a series of images is acquired by camera 1 for each ETL setting with a set of piezo 1 voltage values (moving the piezo over a $\pm 15 \mu\text{m}$ range in steps of 1 μm for each ETL setting). With the reference frame of piezo 1, the z position of the focus generated by the ETL-based manipulation arm for a given ETL current is then determined from the image series, yielding a calibration

function that relates ETL-driver voltage to the z position of the focus in the frame of camera 1.

In the second step, the coordinate system of piezo 2 (which is associated with detection objective 2 and camera 2) is matched to that of piezo 1 (associated with detection objective 1 and camera 1). For this purpose, the ETL is kept at zero power so that the focus spot of the manipulation arm is placed in the native focal plane of detection objective 2, and piezo 1 is positioned at the center of its travel range. Piezo 2 is then moved until the fluorescent focal spot generated by the manipulation arm is in focus on camera 1 and camera 2 at the same time. This configuration is used as a reference when calculating ETL voltage waveforms for experiments with optical manipulation concurrently with volumetric imaging. After this second calibration step, the movements of detection objectives 1 and 2 can be coordinated for simultaneous volumetric imaging from opposing views (for a z range of 200 μm).

In the third step, a set of current values is sequentially applied to the ETL while first piezo 1 and then piezo 2 track the focus of the manipulation arm. For each focus z position, a 2D scan pattern is executed by the galvanometer scanners to generate a grid of focus spots across the field of view (sampling the voltage range -1.2 to $+1.2$ V in steps of 0.24 V to create a grid of size 11×11), while camera 1 acquires an image of the grid. The locations of all spots are determined from the image data to generate a calibration function that relates the voltages applied to the x and y scanners, respectively, to the x and y positions, respectively, of the focus in the frame of cameras 1 and 2.

The calibration functions created in these three steps are inter- and extrapolated to obtain continuous coverage of the full 3D sample volume available to the microscope.

Closed-loop optimization of the ETL control waveform. The calibration functions created by the procedure outlined above serve only as an approximation of the ETL waveforms required to compensate for the piezo movement trajectories used for piezo-based volumetric imaging. The piezo position measured for a given input voltage in a static setting (in which a voltage is applied, and the piezo is given time to settle on the target position) generally differs from that measured for the same voltage in a dynamic setting (such as during the respective phase of a continuous piezo waveform designed for high-speed, piezo-based volumetric imaging). Consequently, effective piezo trajectories in a volumetric-imaging experiment deviate from the expected trajectories projected from the data points obtained from the calibration routine above. Thus, for optimal focus stabilization in the manipulation arm during volumetric imaging, a closed-loop refinement of the ETL waveform is needed. We developed the following six-step procedure for this purpose:

Step 1: A reference image stack of the PSF of the manipulation arm is recorded with high resolution along the z axis (typically with a 200-nm step size). This procedure is accomplished by sweeping a 200- μm z range with piezo 1 while a constant voltage is applied to ETL and piezo 2. Each image in the reference stack is background corrected and thresholded. The xx , xy , and yy moments of inertia (MOIs) are then computed for the thresholded images, thus building a reference table that is subsequently used to match the MOIs associated with the image stream during volumetric imaging in real time. After this reference table is built, any new (live) image can be quickly analyzed to determine the z offset of the current focus position of the manipulation beam requested relative to the stationary reference position.

Step 2: High-speed piezo-based volumetric imaging is performed by sweeping a 200- μm z range with piezo 2 while piezo 1 is kept stationary. The precalculated waveform obtained from the calibration measurement described above is applied to the ETL to cancel out the movement of piezo 2 in first-order approximation. ETL waveforms and temperature readings are stored for each volumetric sweep.

Step 3: While the volumetric-imaging workflow described in step 2 is executed, each image of the z stack acquired at the current time point is subjected to the MOI-processing scheme described in step 1 to obtain the respective xx , xy , and yy MOIs. The reference table constructed from the high-resolution PSF reference stack is used to determine the closest fit and thus the z offset of the current focus position relative to the reference focus position. This computation is performed in real time.

Step 4: The z -offset measurements obtained for each image in the z stack acquired at the previous time point are fitted and resampled to create a voltage-correction curve that is sent to the real-time controller. The correction curve is applied to the ETL voltage waveform for the next time point, minimizing expected z offsets in the next iteration of the volume sweep. The overall goal of this correction step is to achieve a stationary manipulation focus position.

Step 5: Steps 3 and 4 are repeated for a predefined number of time points (see also step 6), such that the correction procedure converges to an optimally fine-tuned ETL waveform that stabilizes the manipulation focus position during volumetric imaging.

Step 6: During this optimization procedure, the ETL temperature is closely monitored, and a zero-voltage setting is used in the short idle time between two consecutive volume scans (for example, the volume scan in a 3-Hz volumetric imaging experiment takes only 250 ms, allowing for an 80 ms ETL idle time between time points) that ensures that the ETL quickly stabilizes at a relatively

low temperature (for the tightly controlled environmental conditions in our microscope room, we observed a reproducible temperature of 23.75 °C after 5 min of continuous imaging with this scheme). The optimized ETL voltage waveform is thus matched to the steady-state operating temperature of the ETL and can be reliably used throughout all subsequent experiments of the same imaging session.

Control of the ETL during volumetric imaging. The ETL driver voltage waveform is calculated right before the execution of each manipulation event, through a four-step procedure:

Step 1: The requested target z position(s) can be defined by the user in the reference frame of either camera 1 or camera 2 (both of which are taken into consideration during the ETL calibration procedure). If camera 2 is used, coordinates are converted to the reference frame of camera 1. Time-dependent, temperature-compensated ETL driver voltages are then computed for the respective target z position(s) during a full volume scan (which may comprise multiple manipulation events) under consideration of the time-dependent piezo 1 positions required for concurrent volumetric imaging.

Step 2: The ETL waveform is shifted in time to consider the relative speed of ETL versus piezo responses to a change in input voltages. Generally, the ETL waveform needs to be delayed relative to the piezo waveform, owing to the slower response time of the latter device.

Step 3: The precalculated ETL waveform is sent to the real-time controller for temporally precise control of voltage levels during the manipulation time window.

Step 4: On the real-time controller, an ETL compensation voltage is added to the ETL waveform right before the execution of each manipulation sequence, on the basis of current ETL temperature readings.

Scripting of manipulation events. We implemented a scripting language for fast and versatile definition of spatiotemporal manipulation events by the user. Scripts are provided to the LabVIEW control framework as text files that define the absolute timing and duration of the manipulation event(s), laser power settings, and the coordinates and geometric shape of the manipulation region(s) (supporting 3D point manipulation as well as more complex shapes, such as circles, spirals, and rectangles). Multiple events can be predefined in each script and automatically executed in sequence with distinct timing definitions (for execution during the same volume scan or spread out in time).

Derivation of focus-shift parameterization for the ETL-based 3D-manipulation arm. The focus shift at the sample can be calculated as a function of the focal-length shift Δf of the ETL (or any type of variable lens) by equating the wavefront sag, or phase change at the edge of the pupil, at each location, i.e., at the variable lens and the objective pupil, respectively. The change in wavefront sag Δs at the edge of the aperture of the variable lens, when operated paraxially ($f \gg r$, where r is half of the aperture diameter), is:

$$\Delta s = \frac{r^2}{2\Delta f} = \frac{r^2}{2} \Delta P \quad (1)$$

Here, $P = 1/f$ is the optical power. At the objective, the correspondence between the sag change at the edge of the pupil and focus shift Δz away from the natural focus, for $\Delta z \ll f_{\text{obj}}$ is:

$$\Delta s = n\Delta z \left(\sqrt{1 - \frac{\text{NA}^2}{n^2}} - 1 \right) \quad (2)$$

Here, n is the index of the immersion medium, and NA is the numerical aperture used for imaging. This expression follows from a geometrical consideration for an objective that satisfies the sine condition.

Equating eqs (1) and (2) gives an approximation of the expression for the focus shift as a function of power change:

$$\Delta z = \frac{r^2}{2n \left(\sqrt{1 - \frac{\text{NA}^2}{n^2}} - 1 \right)} \Delta P \quad (3)$$

This expression depends only on the used aperture size at the variable lens and on the imaging NA and immersion index. Of note, the NA here is not the nominal value of the objective NA but rather the actual imaging NA, which is set by the beam size entering the objective and thus by the beam size (aperture size) at the variable lens and magnification from this lens to the objective.

Characterization of manipulation PSF in fluorescein dye. This section describes the experimental protocol underlying the measurements shown in Fig. 5d. Fluorescence was excited with a pulsed laser beam with a wavelength of 900 nm and an effective numerical aperture of 0.4. The target consisted of an FEP tube with an inner diameter of 2.4 mm and a wall thickness of 25 μm , which was filled with 500 $\mu\text{g/l}$ fluorescein dye in distilled water. A predefined defocus amount ($-100 \mu\text{m}$, $0 \mu\text{m}$, $+100 \mu\text{m}$) was generated by applying a corresponding current to the ETL.

The objective opposite from the one delivering the infrared laser beam to the target was then moved over a 200- μm range in steps of 0.2 μm (with a piezo stage) to acquire a 3D image stack of the PSF. This measurement was repeated at different field positions for each ETL current setting (830 $\mu\text{m} \times 830 \mu\text{m}$ full imaging field of view, measurements labeled as 'center' and 'corner' were performed at distances of 0 μm and 350 μm , respectively, from the center). The numerical aperture of 0.4 was chosen to match the manipulation spot size to our experimental requirements while minimizing optical aberrations introduced by the ETL (by avoiding operating the ETL with large input beams approaching its aperture size).

Volumetric imaging with concurrent 3D optogenetic manipulation.

Zebrafish experiments were conducted according to protocols approved by the Institutional Animal Care and Use Committee of the Howard Hughes Medical Institute, Janelia Research Campus. At 5 dpf, zebrafish larvae from a cross of *Tg(elavl3:jRGECO1b) \times Tg(elavl3:CoChR-eGFP)*, expressing the red calcium indicator jRGECO1b³⁷ and the excitatory opsin CoChR²³ in most neurons, were paralyzed by brief exposure to 100 $\mu\text{g}/\text{ml}$ α -bungarotoxin solution (Life Technologies). The fish were then embedded in 1.4% low-melting-temperature agarose in a glass capillary with a 1.5-mm inner diameter. During gelling of the agarose, each fish was aligned and centered inside the glass capillary by rotation of the capillary and gentle manipulation with Microloader tips (Eppendorf). Just before insertion of the capillary into the microscope sample holder, the fish was positioned above the rim of the glass capillary by extrusion of the agarose cylinder. Finally, the fish was transferred to the microscope sample chamber with its tail pointing down and the dorsal side facing one of the two detection objectives (the same objective through which the femtosecond infrared laser light was delivered for optical perturbation).

Two counterpropagating light sheets with a waist thickness of 3 μm were used to illuminate the fish simultaneously from the left and right sides with a laser wavelength of 561 nm and a power of 90 μW . The fluorescence light collected by the detection objective was filtered and separated from primary excitation light with a long-pass emission filter (LP561, Semrock) combined with a short-pass emission filter (SP680, Semrock). Image acquisition was started after a 30-min resting period for the fish after the transfer to the microscope. Image stacks were acquired at a volume rate of 3 Hz for a volume of 400 $\mu\text{m} \times 800 \mu\text{m} \times 200 \mu\text{m}$ ($x \times y \times z$) with a z-step size of 5 μm (6-ms sweep/exposure time per image, acquiring 41 planes per volume, thus resulting in a 240-ms total acquisition time per volume, followed by a 90-ms rest time, thus yielding a total interval time of 330 ms). We used the AutoPilot framework³⁶ to optimize the spatial overlap of light sheets and the focal plane of the detection objective as a function of the spatial location in the sample. The specimens were imaged in fish-facility water at a temperature of 22 $^{\circ}\text{C}$.

We performed whole-brain volumetric imaging for 5–10 min before initiating 3D optogenetic manipulation to capture spontaneous neuronal activity related to swimming. Those portions of the imaging experiment were then used as a reference for the identification of neurons in three brain regions: the IO, DRN, and the nMfE. Typically, groups of neurons encompassing two cell layers (approximately ten cells per layer, ~20 cells in total) were chosen from each of those three areas, respectively, thus yielding geometrical regions that were larger along the z axis than the 9- μm -long focal volume of the optical manipulation arm. The xyz coordinates of the neurons in each group were extracted from the image data and subsequently used for 3D optogenetic manipulation. To facilitate optical manipulation of each of these areas, cells were targeted consecutively with the laser spot scanning each cell for 4 ms and with a gap time of 1 ms for precisely repositioning the laser with the x- and y-galvanometer scanners. We targeted each cell with a spiral scanning pattern with four revolutions (sampled as 50 points per revolution) and a total diameter of 5 μm . Optical stimulation lasted for 240 ms per time point and was followed by 90 ms of idle time, and was precisely synchronized with image volume acquisition. Each manipulation sequence covered 360 consecutive volume acquisitions (2 min) and was followed by a 2-s time window, in which the femtosecond laser (140-mW power, 950-nm wavelength) was parked at an anterior location outside the brain to support the adaptation of the fish's visual system to the presence of the laser beam. This overall optical manipulation procedure was repeated ten times for each area.

To enable accurate targeting of the selected cells during high-speed volumetric imaging, the ETL (EL-10-30-CI-NIR-LD, Optotune) was programmed to precisely compensate for the motion of detection piezo 2, as described in 'Calibration procedure and control of the ETL-based 3D-manipulation arm in Opto-SiMView' above. To target any depth in the fish brain while the light-sheet microscope scanned over a distance of ~200 μm , the excitation optics were configured such that the focus of the infrared laser beam was adjustable over a z range of ~400 μm (ensuring that the topmost structures could be targeted when imaging from the bottommost structures, and vice versa). During the manipulation idle time after each image volume acquisition, the ETL operating current was set to zero to avoid continuous heating over long time periods. With this approach, the ETL temperature stabilized within 5 min.

For visualizing the brain-wide responses to targeted optogenetic excitation (Fig. 6), we used a color code showing the weighted activity change relative to

control manipulations (manipulations targeted to a set of points outside the brain) to normalize for activity fluctuations not locked to the neuronal stimulation. Specifically, if R_{brain} and R_{outside} are the measured activity changes for manipulations inside and outside the brain, the weighted activity change is defined as $R_{\text{weighted}} = (\text{mean}(R_{\text{brain}}) - \text{mean}(R_{\text{outside}})) / (2(\sigma(R_{\text{brain}}) + \sigma(R_{\text{outside}})))$.

Characterization of the spatial extent of photostimulation during high-speed piezo-based volumetric imaging.

For the experiments shown in Supplementary Figs. 5 and 6, whole-brain imaging of 4-d-old zebrafish larvae expressing PA-GFP^{46,47} under the control of the α -tubulin promoter was performed with two counterpropagating light sheets (488-nm laser wavelength, 3- μm waist thickness) concurrently with the 3D photoactivation of several targets inside the brain. Before photoactivation, spatial overlap of light sheets and detection focal planes were optimized with the AutoPilot framework³⁶. Both before and after photoactivation, anatomy reference stacks were acquired for the 800 $\mu\text{m} \times 415 \mu\text{m} \times 200 \mu\text{m}$ imaging volume with a z-step size of 0.5 μm . Volumetric imaging during photoactivation was performed with the same settings as in Fig. 6 to mimic the typical experimental conditions encountered of an optogenetics experiment (3-Hz volume rate, 5- μm z-step size). For photoactivation during high-speed piezo-based volumetric imaging, targets were illuminated via the microscope's manipulation arm with a laser power of 20 mW (at 900 nm) for superficial regions and 40 mW for deep regions. The photoactivation pulse length per volume scan was set to 250 ms, and photoactivation was performed for eight consecutive volume acquisitions, thus resulting in a total photoactivation time of 2 s.

Reporting Summary. Further information on research design is available in the Nature Research Reporting Summary linked to this article.

Code availability. Our source code is publicly available at <https://github.com/optofish-paper/>. It includes code for creating the brain activity maps from behavioral and calcium imaging data (in Python), a wrapper code for nonrigid registration of zebrafish brains to the reference Z-Brain (Python), an ImageJ plugin for selecting ablation targets (Jython), and code for ablation coordinate correction (Python). The microscope-specific control software (LabVIEW) and software for stimulus presentation and behavior recording (C#) are available upon request (Supplementary Note).

Data availability

Raw data for Fig. 1c are available at <https://github.com/optofish-paper/> (downsampled in space to avoid excessive data size). Example processing steps for Python notebooks are available at the same address. Processed data for Fig. 2 are available at the same address in the form of full brain volumes.

References

- Masino, M. A. & Fetcho, J. R. Fictive swimming motor patterns in wild type and mutant larval zebrafish. *J. Neurophysiol.* **93**, 3177–3188 (2005).
- White, R. M. et al. Transparent adult zebrafish as a tool for in vivo transplantation analysis. *Cell Stem Cell* **2**, 183–189 (2008).
- Chen, T.-W. et al. Ultrasensitive fluorescent proteins for imaging neuronal activity. *Nature* **499**, 295–300 (2013).
- Satou, C. et al. Transgenic tools to characterize neuronal properties of discrete populations of zebrafish neurons. *Development* **140**, 3927–3931 (2013).
- Koyama, M., Kinkhabwala, A., Satou, C., Higashijima, S. & Fetcho, J. Mapping a sensory-motor network onto a structural and functional ground plan in the hindbrain. *Proc. Natl. Acad. Sci. USA* **108**, 1170–1175 (2011).
- Preibisch, S., Saalfeld, S., Schindelin, J. & Tomancak, P. Software for bead-based registration of selective plane illumination microscopy data. *Nat. Methods* **7**, 418–419 (2010).
- Wasserstein, R. L. & Lazar, N. The ASA's statement on p-values: context, process, and purpose. *Am. Stat.* **70**, 129–133 (2016).
- Farcomeni, A. A review of modern multiple hypothesis testing, with particular attention to the false discovery proportion. *Stat. Methods Med. Res.* **17**, 347–388 (2008).
- Zhou, W. et al. Non-sense mutations in the dihydropyridine receptor $\beta 1$ gene, CACNB1, paralyze zebrafish relaxed mutants. *Cell Calcium* **39**, 227–236 (2006).
- Eaton, R. C., Lee, R. K. K. & Foreman, M. B. The Mauthner cell and other identified neurons of the brainstem escape network of fish. *Prog. Neurobiol.* **63**, 467–485 (2001).
- Murphy, D. B. & Davidson, M. W. *Fundamentals of Light Microscopy and Electronic Imaging*. (John Wiley & Sons, Hoboken, NJ, USA, 2012).
- Zipfel, W. R., Williams, R. M. & Webb, W. W. Nonlinear magic: multiphoton microscopy in the biosciences. *Nat. Biotechnol.* **21**, 1369–1377 (2003).
- Avants, B. B. et al. The optimal template effect in hippocampus studies of diseased populations. *Neuroimage* **49**, 2457–2466 (2010).

Reporting Summary

Nature Research wishes to improve the reproducibility of the work that we publish. This form provides structure for consistency and transparency in reporting. For further information on Nature Research policies, see [Authors & Referees](#) and the [Editorial Policy Checklist](#).

Statistical parameters

When statistical analyses are reported, confirm that the following items are present in the relevant location (e.g. figure legend, table legend, main text, or Methods section).

n/a Confirmed

- ☐ ☒ The exact sample size (n) for each experimental group/condition, given as a discrete number and unit of measurement
- ☐ ☒ An indication of whether measurements were taken from distinct samples or whether the same sample was measured repeatedly
- ☐ ☒ The statistical test(s) used AND whether they are one- or two-sided
Only common tests should be described solely by name; describe more complex techniques in the Methods section.
- ☒ ☐ A description of all covariates tested
- ☐ ☒ A description of any assumptions or corrections, such as tests of normality and adjustment for multiple comparisons
- ☐ ☒ A full description of the statistics including central tendency (e.g. means) or other basic estimates (e.g. regression coefficient) AND variation (e.g. standard deviation) or associated estimates of uncertainty (e.g. confidence intervals)
- ☐ ☒ For null hypothesis testing, the test statistic (e.g. F , t , r) with confidence intervals, effect sizes, degrees of freedom and P value noted
Give P values as exact values whenever suitable.
- ☒ ☐ For Bayesian analysis, information on the choice of priors and Markov chain Monte Carlo settings
- ☒ ☐ For hierarchical and complex designs, identification of the appropriate level for tests and full reporting of outcomes
- ☒ ☐ Estimates of effect sizes (e.g. Cohen's d , Pearson's r), indicating how they were calculated
- ☐ ☒ Clearly defined error bars
State explicitly what error bars represent (e.g. SD, SE, CI)

Our web collection on [statistics for biologists](#) may be useful.

Software and code

Policy information about [availability of computer code](#)

Data collection

We used custom LabView code for microscope control and data acquisition, which can be shared upon request.

Data analysis

We make our analysis code publicly available at <https://github.com/optofish-paper>. The registration software ANTs is available at <http://stnava.github.io/ANTs/>.

For manuscripts utilizing custom algorithms or software that are central to the research but not yet described in published literature, software must be made available to editors/reviewers upon request. We strongly encourage code deposition in a community repository (e.g. GitHub). See the Nature Research [guidelines for submitting code & software](#) for further information.

Data

Policy information about [availability of data](#)

All manuscripts must include a [data availability statement](#). This statement should provide the following information, where applicable:

- Accession codes, unique identifiers, or web links for publicly available datasets
- A list of figures that have associated raw data
- A description of any restrictions on data availability

Raw data for Fig. 1c is available at <https://github.com/optofish-paper> (downsampled in space to avoid excessive data size). Example processing steps for Python notebooks are available at the same address. Processed data for Fig. 2 are available at the same address in the form of full brain volumes.

Field-specific reporting

Please select the best fit for your research. If you are not sure, read the appropriate sections before making your selection.

☒ Life sciences ☐ Behavioural & social sciences

For a reference copy of the document with all sections, see [nature.com/authors/policies/ReportingSummary-flat.pdf](https://www.nature.com/authors/policies/ReportingSummary-flat.pdf)

Life sciences

Study design

All studies must disclose on these points even when the disclosure is negative.

Sample size	Sample sizes were chosen to provide enough statistical power to the tests, but keep the experiments reasonable in time and effort. Sample sizes were chosen ahead of time. Statistical corrections for multiple comparisons were applied.
Data exclusions	Fish which behaved erratically (did not swim or did not respond to stimuli) were excluded from imaging and behavior analysis (~25% of animals).
Replication	The results could be replicated across individuals. Statistical corrections for multiple comparisons were applied. We performed control experiments with sham ablations (laser shutter closed), random ablations in the optic tectum (not involved in the tested behavior), and optogenetic stimulus targeted outside the brain.
Randomization	N/A
Blinding	Investigators were not blinded to group allocation.

Materials & experimental systems

Policy information about [availability of materials](#)

n/a	Involvement in the study
<input checked="" type="checkbox"/>	<input type="checkbox"/> Unique materials
<input checked="" type="checkbox"/>	<input type="checkbox"/> Antibodies
<input checked="" type="checkbox"/>	<input type="checkbox"/> Eukaryotic cell lines
<input type="checkbox"/>	<input checked="" type="checkbox"/> Research animals
<input checked="" type="checkbox"/>	<input type="checkbox"/> Human research participants

Research animals

Policy information about [studies involving animals](#); [ARRIVE guidelines](#) recommended for reporting animal research

Animals/animal-derived materials	Experiments were done in accordance with the IACUC of HHMI Janelia Research Campus. Animals were housed in a standard fish facility. The gender of the animals could not be determined at the larval stage. Animals belonged to the species <i>Danio rerio</i> , genetic background nacre, used at 6 days post fertilization.
----------------------------------	---

Method-specific reporting

n/a	Involvement in the study
<input checked="" type="checkbox"/>	<input type="checkbox"/> ChIP-seq
<input checked="" type="checkbox"/>	<input type="checkbox"/> Flow cytometry
<input checked="" type="checkbox"/>	<input type="checkbox"/> Magnetic resonance imaging